

EARLY ONLINE RELEASE

This is a PDF of a manuscript that has been peer-reviewed and accepted for publication. As the article has not yet been formatted, copy edited or proofread, the final published version may be different from the early online release.

This pre-publication manuscript may be downloaded, distributed and used under the provisions of the Creative Commons Attribution 4.0 International (CC BY 4.0) license. It may be cited using the DOI below.

The DOI for this manuscript is

DOI:10.2151/jmsj.2021-077

J-STAGE Advance published date: September 9th, 2021

The final manuscript after publication will replace the preliminary version at the above DOI once it is available.

1 **The o2o3 Local Galerkin Method Using a**
2 **Differentiable Flux Representation**

3 **J. Steppeler**

4 *Climate Service Center, Hamburg, Germany*

5
6 **J. Li**

7 *International Center for Climate and Environment Sciences,*
8 *Institute of Atmospheric Physics, Chinese Academy of*
9 *Sciences, Beijing, China; Department of Applied Mathematics*
10 *and Theoretical Physics, University of Cambridge,*
11 *Cambridgeshire, United Kingdom*

12
13 **F. Fang**

14 *Applied Modelling and Computation Group, Department of*
15 *Earth Science and Engineering, Imperial College London,*
16 *London, United Kingdom*

17

18

J. Zhu

19 *International Center for Climate and Environment Sciences,*
20 *Institute of Atmospheric Physics, Chinese Academy of*
21 *Sciences, Beijing, China; Department of Atmospheric*
22 *Sciences, University of Chinese Academy of Sciences, Beijing,*
23 *China*

24

August 31, 2021

Corresponding author: J. Li, Institute of Atmospheric Physics, Chinese Academy of Sciences, 40 Huayanli, Chaoyang District, Beijing 100029, China.
E-mail: ljx2311@mail.iap.ac.cn

Abstract

The spectral element (SE) and local Galerkin (LG) methods may be regarded as variants and generalizations of the classic Galerkin approach. In this study, the second-order spectral element (SE2) method is compared with the alternative LG scheme referred to as o2o3 that combines a second-order field representation (o2) with a third-order representation of the flux (o3). The full name of o2o3 is o2o3 C^0C^1 , where the continuous basis functions in C^0 -space are used for the field representation and the piecewise third-order differentiable basis functions in C^1 -space are used for the flux approximation. The flux in o2o3 is approximated by a piecewise polynomial function that is both continuous and differentiable, in contrast to many Galerkin and LG schemes that use either continuous or discontinuous basis functions for flux approximations. We show that o2o3 not only has some advantages of SE schemes but also possesses third-order accuracy similar to o3o3 and SE3, while SE2 possesses second-order accuracy and does not show superconvergence. SE3 has an approximation order greater than or equal to three and uses the irregular Gauss-Lobatto collocation grid, while SE2 and o2o3 have a regular collocation grid; this constitutes an advantage for physical parameterizations and follow-up models, such as chemistry or solid-earth models. Furthermore, o2o3 has the technical simplicity of SE2. The common features (accuracy, convergence and numerical dispersion re-

46 lations) and differences between these schemes are described in detail for
47 one-dimensional homogeneous advection tests. A two-dimensional test for
48 cut cells indicates the suitability of o2o3 for realistic applications.

49 **Keywords** Spectral elements (SEs); Local Galerkin (LG); Advection
50 test; Collocation grid

51 **1. Introduction**

52 Some numerical atmospheric models use the classic Galerkin method
53 or its variants to discretize the state variables of the atmospheric motion
54 equations in basis functions. The global spectral method (Simmons et al.
55 1989) uses spherical harmonic basis functions, whereas the finite element
56 (FE) method employs the classic Galerkin method in combination with local
57 basis functions (Steppeler 1987). The advantages of the classic Galerkin FE
58 method include the combination of a high approximation order (third or
59 fourth order) with conservation properties and its suitability for irregular
60 grid structures. Another advantage, namely, a sparse grid, is obtained when
61 the Galerkin method is combined with higher than first-order FEs; in other
62 words, some of the points in the regular grid are omitted, considerably
63 reducing the computational time. For the FE method, such sparse grids are
64 called serendipity grids (Ahlberg et al. 1967).

65 Classic Galerkin methods involve the solution of a linear equation related
66 to the mass matrix. When the matrices are solved by direct methods, such
67 as Gaussian elimination (Steppeler et al. 1990), they require global com-
68 munication, even though the basis functions are local and the mass matrix

69 has a band structure. As classic FE methods require global communication
70 between all cells within the computational domain, it is difficult to scale
71 such models for very large numbers of processors. Accordingly, variants of
72 the classic Galerkin procedure known as local Galerkin (LG) methods were
73 developed (Steppeler and Klemp 2017). In particular, spectral element (SE)
74 techniques are LG methods that have undergone substantial development
75 and are almost suitable for operational use (Herrington et al. 2019). SE
76 methods have achieved scalability for the Nonhydrostatic Unified Model
77 of the Atmosphere (NUMA) for up to millions of processors (Taylor et al.
78 1997; Giraldo 2001; Giraldo and Rosmond 2004; Kelly and Giraldo 2012).
79 The present paper investigates a higher-order LG method referred to as
80 o2o3, the full name of which is o2o3 C^0C^1 . The continuous basis functions
81 for the field representation are piecewise quadratic polynomials in C^0 -space,
82 while third-order differentiable basis functions in C^1 -space are used for the
83 flux approximation. o2o3 C^0C^1 is a further development of the o3o3 C^0C^0
84 method (Steppeler et al. 2019a). Both o2o3 and o3o3 can be considered
85 variants and generalizations of the SE technique. High-order SE methods
86 use the irregular Gauss-Lobatto grid, possibly limiting the time step. Step-
87 peler et al. (2019a) demonstrated that o3o3 inherits the advantages of SEs
88 and allows a larger time step to improve the computational efficiency. Even
89 though the effective resolution of o3o3 as defined by Ullrich et al. (2018) is

90 comparable to that of the third-order spectral element method (referred to
91 as SE3), a dispersion analysis showed that o3o3 has a large 0-space. This
92 means that waves are stationary for a relatively large range of wavenumbers.

93 Classic Galerkin approaches are widely applied in computational fluid
94 dynamics (CFD), where irregular cells are used to correctly describe the
95 surface of an airplane. In a meteorological context, this property may trans-
96 late into an accurate representation of the lower surface, meaning a more
97 accurate approximation of mountains. Additionally, FEs are expected to
98 improve the impact of mountains on atmospheric circulation. For meteoro-
99 logical models, it is important for the lines composed of grid points to be
100 horizontally aligned (Steppeler et al. 2006). Hence, these horizontal lines
101 of grid points cut into the mountains. However, the lower boundary rep-
102 resentation is complex, which hinders the use of this approach during the
103 modeling process. Terrain-following coordinates enable the alignment of the
104 grids with the surface topography, thereby simplifying the computation of
105 the lower boundary condition (Phillips 1957). Horizontally aligned grids are
106 normally constructed using a regular height grid structure where only the
107 surface grid cells are irregular (Yamazaki and Satomura 2010). The hori-
108 zontal alignment of numerical grids and the underlying terrain, such as that
109 obtained with cut cells (Nishikawa and Satoh 2016), will result in a more
110 accurate representation of mountains (Steppeler et al. 2006; Zängl 2012).

111 Steppeler et al. (2019b) showed that cut cells provide a better represen-
112 tation of vertical velocities in a three-dimensional realistic model than the
113 models using terrain-following coordinates, leading to improved forecasts.
114 Consequently, cut-cell models were used with grid point numerical methods
115 (Yamazaki et al. 2016; Steppeler et al. 2019b).

116 Steppeler and Klemp (2017) showed that some finite-difference (FD)
117 cut-cell approximations can produce noisy solutions even for smooth moun-
118 tains. Their work was limited to linear test functions and a rather simple
119 test mountain consisting of a straight line. However, SE and FE methods
120 are mostly performed on grids that are not horizontally aligned (Marras
121 et al. 2016). Therefore, the advantages of cut cells in representing moun-
122 tains proposed by Steppeler and Klemp (2017) are not realized with these
123 FE/SE representations. In contrast, Galerkin methods using first-order ba-
124 sis functions and horizontally aligned grids lead to solutions without such
125 noise (Steppeler and Klemp 2017). This finding confirms the fact that
126 Galerkin methods lead to accurate surface approximations when the cells
127 are adapted to the surface, meaning for horizontally aligned cells. Nev-
128 ertheless, existing atmospheric Galerkin models often do not take advan-
129 tage of such suitability for good surface approximations, because grids that
130 are not horizontally aligned are typically used. A notable exception is
131 the atmospheric model called Active Tracer High-resolution Atmospheric

132 Model-Fluidity (ATHAM-Fluidity) that uses horizontally aligned cells and
133 achieves good results in the generation of mountain-induced waves (Savre
134 et al. 2016).

135 In this study, we construct o2o3 to address the disadvantages of o3o3,
136 and we demonstrate the following properties of o2o3:

- 137 • The accuracy of o2o3 is comparable to that of SE3 as a result of
138 the constructed superconvergence, even though o2o3 has the simplic-
139 ity and basis function structure of the second-order spectral element
140 method (referred to as SE2).
- 141 • o2o3 uses a regular collocation grid, while SE3 uses the irregular
142 Gauss-Lobatto grid; the former is an advantage when parameteriz-
143 ing physical processes (Herrington et al. 2019).
- 144 • A sparse grid is possible with o2o3, while SE3 uses a full grid.
- 145 • o2o3 avoids the large 0-space of o3o3.
- 146 • The suitability of the high-order o2o3 method for cut cells is shown
147 using the simple example of Steppeler and Klemp (2017). Therefore,
148 o2o3 allows for cut-cell implementation in second- and third-order
149 spaces, while the Steppeler and Klemp (2017) scheme uses linear basis
150 functions.

151 We describe the grid and approximation spaces for SE2, o2o3, and SE3
152 in Section 2. A summary of the numerical properties of all schemes com-
153 pared in this paper is given in Tab. 1. Section 3 outlines the inhomogeneous
154 FD schemes representing the approximations of these schemes. Section 4
155 presents the LG procedure for o2o3, conserving first-order moments. Sec-
156 tion 5 illustrates the results of a homogeneous advection test to show the
157 accuracy and stability, convergence and numerical dispersion relations of
158 o2o3, and the study is concluded in Section 6.

Table 1

159 2. Grids and approximation spaces

160 In this study, the test problem involves homogeneous one-dimensional
161 (1D) advection of the density field $h(x)$:

$$\frac{\partial h}{\partial t} = -u_0 \frac{\partial h}{\partial x}, \quad (1)$$

162 where u_0 is the velocity field, assumed to be constant, and the periodic
163 boundary condition is imposed.

164 Eq. (1) is solved using piecewise polynomial spaces of degrees 2 and
165 3. These are the discretization spaces used with the continuous Galerkin
166 schemes o2o3, SE2, and SE3. Let a 1D domain Ω be divided into the el-
167 ements $\Omega_i (i = 0, 1, 2, \dots)$, where $\Omega_i = (x_i, x_{i+1})$. In each element Ω_i , the
168 polynomial $P_i(x) = \sum_{j=0}^J p_{i,j} x^j$ is determined by three polynomial coeffi-

169 cients $p_{i,0}, p_{i,1}, p_{i,2}$ for SE2 and by four coefficients $p_{i,0}, p_{i,1}, p_{i,2}, p_{i,3}$ for SE3.
 170 The index i indicates that the polynomial representation is applicable to
 171 the element Ω_i . Therefore, for a discontinuous second-order field represen-
 172 tation, the polynomial coefficients $p_{i,0}, p_{i,1}, p_{i,2}$ are independently chosen and
 173 are the degrees of freedom. The spaces formed by $p_{i,0}, p_{i,1}, p_{i,2}, p_{i,3}$ are used
 174 for third-order discontinuous and continuous field representations. For the
 175 continuous Galerkin scheme, the polynomials need to fit together continu-
 176 ously, implying the condition $P_{i-1}(x_i) = P_i(x_i)$ and $P_i(x_{i+1}) = P_{i+1}(x_{i+1})$.
 177 Therefore, we have only two degrees of freedom per element with SE2 and
 178 three for SE3.

Fig. 1

179 In one dimension, the length of the element Ω_i is defined as $dx_i = x_{i+1} -$
 180 x_i . If the grid distribution is regular, then $dx = dx_i$. The boundary grid
 181 points x_i and x_{i+1} of the element Ω_i are called the principal points or corner
 182 points. For SE2, there are three independent amplitudes described by three
 183 collocation point values in each element, while there are four amplitudes for
 184 SE3 (Fig. 1). Collocation points are grid points within an element such that
 185 the amplitudes at these points are sufficient to determine the polynomial
 186 coefficients corresponding to this element. For SE2 and o2o3, the fields are
 187 quadratic polynomials within the element Ω_i , and we need three collocation
 188 points $X_{i,0}, X_{i,1}, X_{i,2}$. Even though we have three collocation points per
 189 element, the dimension of the collocation grid space is twice as large as the

190 number of elements, as principal points are shared by two elements. For a
 191 third-order field representation, such as with SE3 or the flux for o2o3, we
 192 need two interior points in addition to two principal points. Therefore, the
 193 collocation grid points are $X_{i,j}$ ($i = 0, 1, 2, \dots, j = 0, 1, \dots, J$) in Ω_i :

$$\begin{cases} X_{i,0} = x_i, X_{i,1} = x_i^m, X_{i,2} = x_{i+1}, & \text{for SE2 and o2o3 ,} \\ X_{i,0} = x_i, X_{i,1} = x_i^m - \frac{1}{2\sqrt{5}}dx_i, X_{i,2} = x_i^m + \frac{1}{2\sqrt{5}}dx_i, X_{i,3} = x_{i+1}, & \text{for SE3 ,} \end{cases} \quad (2)$$

194 where $x_i^m = \frac{1}{2}(x_i + x_{i+1})$ is the midpoint of the element Ω_i . We have $J = 2$
 195 for o2o3 and SE2 and $J = 3$ for SE3. The collocation grids X are noted by
 196 broken indices: $x_{i+\frac{1}{2}} = X_{i,1}$ for SE2 and o2o3 and $x_{i+\frac{1}{3}} = X_{i,1}$, $x_{i+\frac{2}{3}} = X_{i,2}$
 197 for SE3. We note that in Eq. (2), the collocation points form a set of
 198 Gauss-Lobatto points of either three (SE2 or o2o3) or four (SE3) nodes.
 199 The sets of points are redundant as follows:

$$\begin{cases} X_{i,2} = X_{i+1,0} = x_{i+1}, & \text{for SE2 and o2o3 ,} \\ X_{i,3} = X_{i+1,0} = x_{i+1}, & \text{for SE3 .} \end{cases} \quad (3)$$

200 The field values at collocation points form the grid point space. The
 201 points $X_{i,j}$ must be used to derive the initial data for the three schemes.

202 The basis functions used to define the field $h(x)$ in Eq. (1) are the same
 203 among the three schemes. The basis functions are defined in the interval

204 $(x_i^m - \frac{1}{2}dx_i, x_i^m + \frac{1}{2}dx_i)$ as follows:

$$\left\{ \begin{array}{l} e_i^+(x) = \frac{1}{2} + \frac{1}{dx_i}(x - x_i^m), \\ e_i^-(x) = \frac{1}{2} - \frac{1}{dx_i}(x - x_i^m), \\ b_i^2(x) = \frac{1}{2} [(x - x_i^m)^2 - \frac{1}{4}dx_i^2], \\ b_i^3(x) = \frac{1}{6} [(x - x_i^m)^3 - \frac{1}{4}(x - x_i^m)dx_i^2]. \end{array} \right. \quad (4)$$

205 These four basis functions are identically zero when $x \notin (x_i^m - \frac{1}{2}dx_i, x_i^m +$
 206 $\frac{1}{2}dx_i)$.

207 For any field or flux $q(x)$, we can derive the discretized representation
 208 using the basis functions defined in Eq. (4):

$$q(x) = \left\{ \begin{array}{l} \sum_{i=0,1,2,\dots} q_{i+1}^- e_{i+1}^+(x) + q_i^+ e_i^-(x) + q_{xx,i+\frac{1}{2}} b_i^2(x) + \varepsilon q_{xxx,i+\frac{1}{2}} b_i^3(x), \quad \text{for SE2 and o2o3,} \\ \sum_{i=0,1,2,\dots} q_{i+1}^- e_{i+1}^+(x) + q_i^+ e_i^-(x) + q_{xx,i+\frac{1}{2}} b_i^2(x) + q_{xxx,i+\frac{1}{2}} b_i^3(x), \quad \text{for SE3,} \end{array} \right. \quad (5)$$

209 where $\varepsilon = 0$ is used for the second-order field representation with SE2 and
 210 o2o3, while $\varepsilon = 1$ is used for the flux in the third-order representation with
 211 o2o3. For the representation of discontinuous functions, two values of $q(x)$
 212 at principal nodes are introduced: q_i^+ and q_i^- . We note that in this study,
 213 discontinuous functions occur for flux derivatives with SE2 and SE3. In Eq.
 214 (5), the amplitudes $q_i, q_{xx,i+\frac{1}{2}}$ form the spectral space for SE2 and o2o3,

215 whereas the amplitudes $q_i, q_{xx,i+\frac{1}{2}}, q_{xxx,i+\frac{1}{2}}$ form the spectral space for SE3.
 216 For the field $q(x)$, the grid point space for SE2 and o2o3 is formed by q_i
 217 and $q_{i+\frac{1}{2}}$ ($i = 0, 1, 2, 3, \dots$). According to Eq. (5), q_i at the principal nodes
 218 represents both the spectral amplitudes and the grid point values for the
 219 three schemes.

220 Using Eq. (5), we can obtain the transformation equations to the grid
 221 point space at the midpoints $x_{i+\frac{1}{2}}$ for SE2 and o2o3 with $\varepsilon = 0$:

$$q_{i+\frac{1}{2}} = q_{xx,i+\frac{1}{2}} b^2(x_{i+\frac{1}{2}}) + \frac{1}{2}(q_i + q_{i+1}) = -\frac{1}{8}q_{xx,i+\frac{1}{2}} dx_i^2 + \frac{1}{2}(q_i + q_{i+1}). \quad (6)$$

222 From Eq. (6), we can obtain the transformation from the grid point space
 223 to the spectral space in Ω_i . When q_i, q_{i+1} and $q_{i+\frac{1}{2}}$ are given, the transfor-
 224 mation to the spectral space is:

$$q_{xx,i+\frac{1}{2}} = -\frac{4}{dx_i^2} \left[2q_{i+\frac{1}{2}} - (q_i + q_{i+1}) \right]. \quad (7)$$

225 For the third-order space used in SE3, we refer to Steppeler et al. (2019a)
 226 for the formulas of the transformation between the grid point space and
 227 spectral space. A list of published LG schemes and their discretization
 228 spaces is given in Tab. 1.

229 We note that o2o3 for the two-dimensional (2D) problem is obtained by
 230 differencing along the coordinate lines, analogous to the 2D o3o3 scheme

231 derived in Steppeler et al. (2019a). Therefore, the 1D scheme is extracted
232 while leaving the interior points out. Thus, the 2D grid becomes sparse for
233 interior points that are not used for forecasting. This means that the sparse
234 grid is obtained from the full grid (all points are dynamic) by removing
235 the interior points, as illustrated in Fig. 2. Thus, only the grid points
236 at the corners and edges are dynamic. Steppeler et al. (2019a) defined
237 the sparseness factor as the ratio of the number of dynamic points to the
238 number of points in the full grid. A small sparseness factor indicates the
239 potential for reducing the computational time.

Fig. 2

240 3. Inhomogeneous finite difference schemes

241 The classic fourth-order FD scheme (o4) is a homogeneous FD scheme
242 that uses the same FD formula at each grid point. In contrast, SE and
243 other LG schemes typically use different discretization equations at each
244 collocation point (Steppeler et al., 2019a); these approaches are known as
245 an inhomogeneous FD scheme. In this section, we discuss inhomogeneous
246 FD schemes resulting in the temporal derivatives of the field $q(x)$ for a
247 regular grid distribution $dx_i = dx$.

248 SE2, o2o3, and SE3 are used as examples for comparison. For all three
249 examples, $q(x)$ within the cells is approximated by polynomials. For any of
250 the collocation points, these polynomials are not centered around the target

251 point (the point to compute the derivatives). Rather, to obtain the spatial
 252 derivative of $q(x)$ in a cell, the polynomial is differentiated at different col-
 253 location points. We note that the right and left derivatives ($q_{x,i}^+$ and $q_{x,i}^-$) at
 254 the principal points are defined discontinuously between two different cells;
 255 thus, an averaging procedure for $q_{x,i}^+$ and $q_{x,i}^-$ must be defined to obtain $q_{x,i}$.
 256 Therefore, the FD schemes in a cell differ among the collocation points, and
 257 as a consequence, the three schemes are inhomogeneous in the grid point
 258 space. In the following paragraphs, we introduce three schemes for both
 259 principal and interior points except that o2o3 for the interior points will be
 260 defined in the next section.

261 For SE2, the time derivative in Eq. (1) at the collocation points can be
 262 computed using the field representation Eq. (5) with $\varepsilon = 0$. For the interior
 263 points in Ω_i , the functional representation in Eq. (5) is differentiable, and
 264 we can obtain:

$$\begin{aligned}
 q_{t,i+\frac{1}{2}} &= -u_0 q_{x,i+\frac{1}{2}} = -u_0 \left[q_{i+1} e_{x,i+1}^+(x_i^m) + q_i e_{x,i}^-(x_i^m) + q_{xx,i+\frac{1}{2}} b_{x,i}^2(x_i^m) \right] \\
 &= -u_0 \frac{q_{i+1} - q_i}{dx},
 \end{aligned} \tag{8}$$

265 where $b_{x,i}^2(x_i^m) = 0$.

266 For the principal points x_i in Ω_i , the basis function in Eq. (4) has a
 267 discontinuous derivative, and we obtain the right and left derivatives, $q_{x,i}^+$

268 and $q_{x,i}^-$ at x_i from Eq. (5). These values are obtained as follows:

$$\begin{cases} q_{x,i}^+ = \frac{q_{i+1}-q_i}{dx} + q_{xx,i+\frac{1}{2}} b_{x,i}^2(x_i) = \frac{q_{i+1}-q_i}{dx} + \frac{4}{dx} \left(q_{i+\frac{1}{2}} - \frac{q_{i+1}+q_i}{2} \right), \\ q_{x,i}^- = \frac{q_i-q_{i-1}}{dx} + q_{xx,i-\frac{1}{2}} b_{x,i}^2(x_i) = \frac{q_i-q_{i-1}}{dx} - \frac{4}{dx} \left(q_{i-\frac{1}{2}} - \frac{q_i+q_{i-1}}{2} \right), \end{cases} \quad (9)$$

269 where we use the transformation formula for the spectral space and Eqs.
270 (4), (5) and (7).

271 If the derivative at a principal node is defined as the average of these
272 two values, we can write $q_{t,i}$ as:

$$q_{t,i} = -\frac{u_0}{2}(q_{x,i}^+ + q_{x,i}^-) = -u_0 \left(-\frac{q_{i+1} - q_{i-1}}{2dx} + 2\frac{q_{i+\frac{1}{2}} - q_{i-\frac{1}{2}}}{dx} \right). \quad (10)$$

273 The right-hand-side term in Eq. (10) is a linear combination of two cen-
274 tered FD schemes with second-order accuracy. By comparing Eq. (8) with
275 Eq. (10), this scheme can be recognized as an inhomogeneous FD scheme.
276 Because neither Eq. (8) nor Eq. (10) has an approximation order higher
277 than two, superconvergence does not occur for SE2.

278 o2o3 may be viewed as a generalization of SE2 with constructed inherent
279 superconvergence to an order of at least three. Therefore, o2o3 will be
280 introduced as an inhomogeneous FD scheme. For the principal grid points
281 in Ω_i , any FD scheme of at least the third order may be chosen. Here, we
282 choose the classic o4 scheme:

$$q_{t,i} = -u_0 \left(-\frac{1}{3} \frac{q_{i+1} - q_{i-1}}{2dx} + \frac{4}{3} \frac{q_{i+\frac{1}{2}} - q_{i-\frac{1}{2}}}{dx} \right), \quad (11)$$

283 for the derivatives at the principal nodes in Ω_i .

284 Eq. (11) guarantees fourth-order accuracy at corner points on regular
 285 grids (Durran 2010). However, for irregular grids, the accuracy drops to
 286 the first order. Now, we list the formula for calculating q_t on an irregular
 287 grid. When we employ Eq. (11) for all points, the rather strong deviation
 288 from conservation occurs partly due to a decrease in the order of approxima-
 289 tion to 1. This decrease in the order of approximation is then counteracted
 290 by smoothly changing the resolution. Grid smoothing methods, such as
 291 “spring dynamics” (Tomita et al. 2001), are applied, while the Voronoi
 292 type of smoothed grid is used for the Model for Prediction Across Scales
 293 (MPAS) (Skamarock et al. 2012). For irregular grid structures, an alter-
 294 native generalized formulation of Eq. (11) is derived as (Steppeler et al.
 295 2008):

$$q_t(x_i) = w_i^{-1} q_{i-1} + w_i^{-\frac{1}{2}} q_{i-\frac{1}{2}} + w_i q_i + w_i^{\frac{1}{2}} q_{i+\frac{1}{2}} + w_i^1 q_{i+1}, \quad (12)$$

296 where the corresponding weights w_i shown in Tab. 2 are computed numer-
 297 ically, for example, by polynomial fitting in Steppeler et al. (2019a). A
 298 simplification is achieved by replacing the Legendre representation of the
 299 polynomial space with order-consistent polynomials. Any other high-order

300 FD scheme can be used as an alternative to Eq. (11) or Eq. (12). In the
 301 following text, we refer to the o4 scheme given by Eq. (11) as classic o4,
 302 while the o4 scheme given by Eq. (12) is referred to as weighted o4. We
 303 consider an example of irregular grids as defined in the seventh column of
 304 Tab. 2 (see also Section 5.1). With these weights, a third-order approxi-
 305 mation can be achieved when we apply the differentiation to analytic test
 306 functions, such as polynomials of degree 3. We note that the value of w_i
 307 in the fine mesh area ($dx = 1$) is twice the value in the coarse mesh area
 308 ($dx = 2$). The advantages of Eq. (12) will be demonstrated in Section 5.1.

Table 2

309 For comparison purposes, we also use SE3. For the principal nodes in
 310 SE3, averaging between right and left values, as performed in Eq. (10), is
 311 adapted to the third-order representation. For the two interior nodes, Eq.
 312 (8) is used analogously because the basis function representation for SE3 is
 313 directly differentiated.

314 Finally, the proof of the third-order approximation of Eq. (11) follows
 315 from the requirement of third-order consistency. The FD equation for mass
 316 follows directly from Eq. (5). Let dm_i be the mass contained in the element
 317 $\Omega_i = (x_i, x_{i+1})$:

$$dm_i = \int_{x_i}^{x_{i+1}} q(x) dx. \quad (13)$$

318 Then, we have:

$$dm_i = \frac{dx}{2}(q_i + q_{i+1}) + \frac{2}{3}dx \left(q_{i+\frac{1}{2}} - \frac{q_{i+1} + q_i}{2} \right). \quad (14)$$

319 The mass conservation property requires that the time derivative of the
 320 mass of dm_i within the element Ω_i is the flux difference at the two principal
 321 points of the element Ω_i . We show this in the next section.

322 4. Local Galerkin procedure

323 In this section, with the field representation defined in Section 2, we
 324 introduce the LG procedure to define o2o3 in comparison with SE2 and
 325 SE3.

326 We assume $h(x)$ to be represented in the grid point space by h_i , and
 327 we assume that $h(x)$ can be transformed into the spectral space by Eq.
 328 (7). This will result in the spectral amplitudes $h_i, h_{xx,i+\frac{1}{2}}$ for SE2 and o2o3
 329 and the spectral amplitudes $h_i, h_{xx,i+\frac{1}{2}}, h_{xxx,i+\frac{1}{2}}$ for SE3 in Ω_i . Using these
 330 amplitudes, Eq. (5) gives the functional form of $h(x)$.

331 For SE2 and SE3, $fl(x) = -u_0h(x)$ can be defined using the represen-
 332 tations in Eqs. (5) and (7). For SE2, we have:

$$\begin{cases} fl_i = -u_0h_i, \\ fl_{xx,i+\frac{1}{2}} = -u_0h_{xx,i+\frac{1}{2}}. \end{cases} \quad (15)$$

333 For SE3, we refer to Eqs. (5) and (7) analogously:

$$\left\{ \begin{array}{l}
 fl_i = -u_0 h_i, \\
 fl_{xx,i+\frac{1}{2}} = -u_0 h_{xx,i+\frac{1}{2}}, \\
 fl_{xxx,i+\frac{1}{2}} = -u_0 h_{xxx,i+\frac{1}{2}}.
 \end{array} \right. \quad (16)$$

334 We note that in this study, discontinuous functions occur for flux derivatives
 335 with SE2 and SE3.

336 To define o2o3, the temporal derivative of the field is proportional to the
 337 spatial derivative according to Eq. (1), which means that we only need to
 338 determine the expressions of $h_{t,i} = fl_{x,i}$ at the principal nodes and of $fl_{xx,i+\frac{1}{2}}$
 339 and $fl_{xxx,i+\frac{1}{2}}$ at the interior nodes within Ω_i . However, in o2o3, the field
 340 $h(x)$ given by Eq. (5) has only a second-order representation. Therefore,
 341 we apply Eq. (5) with $\varepsilon = 1$ to define a third-order representation of the
 342 flux $fl(x)$.

343 At the principal nodes in Ω_i with o2o3, we again define:

$$fl_i = -u_0 h_i, \quad (17)$$

344 which will not be used, as we are interested only in the flux divergence
 345 used in Eq. (1), rather than in the value of the flux itself. The third-
 346 order flux representation according to Eq. (11) is defined such that $fl(x)$
 347 is differentiable at the principal nodes of Ω_i . The degree-3 polynomial is

348 defined such that the derivatives at the principal points have the same value
 349 for left and right differentiation. Therefore, by construction, we obtain a
 350 differentiable spline. The derivative $fl_{x,i}$ at the principal nodes of $fl(x)$ is
 351 defined analogously to Eq. (11) up to a classic o4 approximation:

$$fl_{x,i} = -u_0 \left(-\frac{1}{3} \frac{h_{i+1} - h_{i-1}}{2dx} + \frac{4}{3} \frac{h_{i+\frac{1}{2}} - h_{i-\frac{1}{2}}}{dx} \right). \quad (18)$$

352 We note that the definition in Eq. (18) already gives the FD equations at
 353 the principal nodes according to Eq. (1):

$$h_{t,i} = fl_{x,i}. \quad (19)$$

354 At the interior points within the element Ω_i , the values of $fl_{xx,i+\frac{1}{2}}$ and
 355 $fl_{xxx,i+\frac{1}{2}}$ follow the continuity requirement of the functional representation
 356 in Eq. (11) at the principal nodes (see the details of the steps to derive the
 357 time derivative of $h(x)$ in Fig. 3). We provide two methods to obtain the
 358 expressions of $fl_{xx,i+\frac{1}{2}}$ and $fl_{xxx,i+\frac{1}{2}}$. Fig. 3

359 In the first method, the equations for the spectral coefficients $fl_{xx,i+\frac{1}{2}}$
 360 and $fl_{xxx,i+\frac{1}{2}}$ are obtained by taking the x -derivative of Eq. (5):

$$\begin{cases} fl_{x,i} = fl_{i+1}e_{x,i+1}^+(x_i) + fl_i e_{x,i}^-(x_i) + fl_{xx,i+\frac{1}{2}}b_{x,i}^2(x_i) + fl_{xxx,i+\frac{1}{2}}b_{x,i}^3(x_i), \\ fl_{x,i+1} = fl_{i+1}e_{x,i+1}^+(x_{i+1}) + fl_i e_{x,i}^-(x_{i+1}) + fl_{xx,i+\frac{1}{2}}b_{x,i}^2(x_{i+1}) + fl_{xxx,i+\frac{1}{2}}b_{x,i}^3(x_{i+1}). \end{cases} \quad (20)$$

361 Eq. (20) is an equation for $fl_{xx,i+\frac{1}{2}}$ and $fl_{xxx,i+\frac{1}{2}}$, as all other quantities
 362 are known. The derivatives of $e_{i+1}^+, e_i^-, b_i^2, b_i^3$ are obtained from their defini-
 363 tions in Eq. (4). Using Eqs. (4), (5) and (20), we can derive the expressions
 364 for the spectral amplitudes at the interior points $x_{i+\frac{1}{2}}$:

$$fl_{xx,i+\frac{1}{2}} = \frac{1}{dx}(fl_{x,i+1} - fl_{x,i}), \quad (21)$$

365 and

$$fl_{xxx,i+\frac{1}{2}} = \frac{6}{dx^2}[fl_{x,i+1} + fl_{x,i} - \frac{2}{dx}(fl_{i+1} - fl_i)]. \quad (22)$$

366 For the time derivative at the interior point of an element, according to
 367 $b_{x,i}^3(x_{i+\frac{1}{2}}) = -\frac{1}{24}dx^2$ and Eqs. (4), (5), (21) and (22), we can obtain:

$$\begin{aligned} h_{t,i+\frac{1}{2}} &= fl_{x,i+\frac{1}{2}} \\ &= fl_{i+1}e_{x,i+1}^+(x_{i+\frac{1}{2}}) + fl_i e_{x,i}^+(x_{i+\frac{1}{2}}) + fl_{xx,i+\frac{1}{2}}b_{x,i}^2(x_{i+\frac{1}{2}}) + fl_{xxx,i+\frac{1}{2}}b_{x,i}^3(x_{i+\frac{1}{2}}) \\ &= \frac{3}{2} \frac{fl_{i+1} - fl_i}{dx} - \frac{1}{2} \frac{fl_{x,i+1} + fl_{x,i}}{2}. \end{aligned} \quad (23)$$

368 In the second method, we directly employ the principle of the conser-
 369 vation of mass to construct Eq. (23). Let the time derivative of h at the
 370 principal nodes be given again by Eq. (19) or by any other difference scheme
 371 of at least the third order. By differentiating Eq. (14) with respect to t , the
 372 time derivative of the mass $dm_{t,i}$ in the element Ω_i is obtained as:

$$dm_{t,i} = \frac{dx}{2}(h_{t,i} + h_{t,i+1}) + \frac{2}{3}dx \left(h_{t,i+\frac{1}{2}} - \frac{h_{t,i} + h_{t,i+1}}{2} \right). \quad (24)$$

373 $dm_{t,i}$ can also be computed from the flux into Ω_i , and we obtain:

$$dm_{t,i} = -u_0(h_{i+1} - h_i). \quad (25)$$

374 By combining Eqs. (24) and (25) and solving for $h_{t,i+\frac{1}{2}}$, we obtain Eq. (23).

375 These two methods lead to the same piecewise quadratic polynomial repre-
 376 sentation. The uniqueness of the two methods follows from the fact that the
 377 equation of motion is assumed to be valid with the spatial flux representa-
 378 tion as a piecewise cubic spline. The derivation of Eq. (23) from the basis
 379 function representation implies the conservation of first-order moments, cor-
 380 responding to the conservation of mass in this case. Therefore, Eqs. (23)
 381 and (18) can be viewed as a method for defining the time derivative $h_{t,i}$
 382 such that mass is conserved.

383 Fig. 3 illustrates the steps for the computation of the time derivative
 384 of the field h . The field is defined as $h(x_i) = 0$, except for $h(x_{500}) = 4$.
 385 This defines a rather small-scale field for which different numerical methods
 386 are expected to give different results. For smooth fields, all methods must
 387 give very similar results. Fig. 3a shows the results with SE2. The flux
 388 in this case that is shown as the dashed curve is merely the negative of
 389 the field. However, the spatial derivative of the flux shown by the dotted

390 line, is discontinuous. The blue curve is the result of the LG operation that
 391 approximates the derivative by a continuous function. Fig. 3b shows similar
 392 results for o2o3. The flux shown by the dashed curve is approximated by a
 393 differentiable function, and the spatial derivative of the flux shown by the
 394 dotted curve is continuous; hence, no further approximation is necessary.
 395 Fig. 3c gives the result for SE3, which is analogous to the result shown in
 396 Fig. 3a, but with the approximating polynomial of degree 3. We note that
 397 the grid is different from that of SE2 because its length is $3dx$.

398 For all of the described methods, when the time derivative $h_t(x)$ is given
 399 in the grid point space, the fourth-order Runge-Kutta method (RK4) can
 400 be applied as with any other FD scheme. Although the example of Fig. 3
 401 uses a low resolution, all methods give a reasonable approximation of the
 402 time derivative. This is important, as practical calculations in meteorology
 403 depend on reasonable approximations with poor resolution in some instances
 404 (Steppeler et al. 2003), and the orography is often not well-resolved in
 405 atmospheric models.

406 Thus far, we have already illustrated how to generate the inhomogeneous
 407 o2o3 scheme for $h_{t,i}$ and $h_{t,i+\frac{1}{2}}$ using the homogeneous 1D advection equa-
 408 tion Eq. (1). Overall, the steps of the implementation of o2o3 are described
 409 as follows:

- 410 • Step 1: Divide the computational domain (Fig. 1) into elements and

411 define the collocation points Eq. (2) in each element. Note that the
412 collocation points include the corner point and interior point for o2o3;

413 • Step 2: Define the basis functions Eq. (4) for the field representation
414 and flux representation Eq. (5) in each element;

415 • Step 3: Construct the temporal derivative of field $h_{t,i}$ Eq. (19) at
416 corner points by Eqs. (1) and (17) and a classic o4 scheme Eq. (18);

417 • Step 4: Construct the temporal derivative of field $h_{t,i+\frac{1}{2}}$ at interior
418 points by Eq. (23) or the condition of flux conservation expressed
419 by Eqs. (24)-(25). Note that to achieve the variable $h_{t,i+\frac{1}{2}}$, we need
420 to rely on the intermediate variables: the second- and third-spatial
421 derivatives of the flux at the interior point expressed by Eqs. (21)-
422 (22);

423 • Step 5: Compute h_i and $h_{i+\frac{1}{2}}$ at the next time level using the RK4
424 method or any proper time integration scheme.

425 Note that the time loop consists of Steps 3, 4 and 5. Steps 1 and 2 are used
426 to initialize the forecast.

427 5. Results

428 To investigate the characteristics of o2o3, including its accuracy, conver-
429 gence, numerical dispersion and stability, homogeneous advection tests in
430 both one and two dimensions are implemented. For a first examination of
431 the suitability of o2o3 for high-order cut-cell modelling, an advection test
432 along a straight mountain is implemented.

433 5.1 1D homogeneous advection test

434 The advection equation in Eq. (1) is solved for a 1D area with 600
435 points, and the constant-velocity field u_0 is set to be $u_0 = 1.0$. For o2o3
436 and SE2, 300 elements are present in the area, while for SE3, 200 elements
437 are present.

438 With an element length $dx = 2$ for o2o3 and SE2, the resolution of the
439 collocation grid is $dx^r = 1$. Tab. 3 shows the Courant-Friedrichs-Lewy
440 (CFL) condition with RK4 time-stepping. The available time steps (i.e.,
441 CFL condition) are 2.2, 1.8 and 1.5 for SE2, o2o3 and SE3, respectively.
442 According to conventional wisdom (Durrant 2010), classic o4 has a stability
443 limit of 1.9 with the RK4 scheme. This means that o2o3 has a marginally
444 smaller CFL condition than the classic o4 scheme. The relatively weak
445 CFL condition with SE3 can be explained by the minimum grid size of the
446 Gauss-Lobatto grid being lower than that of the equally spaced grid used

447 with o2o3. Therefore, the time step in o2o3 is approximately 20% higher
 448 than that in SE3. However, these two schemes are comparable with regard
 449 to their accuracy and conservation properties. The large CFL number of
 450 SE2 is to be expected, as the transition to a higher order often requires a
 451 smaller time step. Ultimately, the CFL conditions for o2o3, SE2, and SE3
 452 are more severe than those for the second-order centered FD scheme.

Table 3

453 To measure stability, we perform temporal integration for a long time.
 454 We use $\frac{30000}{dt}$ steps, meaning that the structure is transported over 30000 grid
 455 points or 15000 elements over the area. Because of the periodic boundary
 456 conditions, for $t = 600 n$ ($n = 1, 2, 3, \dots$), the analytic solution of Eq. (1) is
 457 identical to the initial value, so that the accuracy can easily be checked at
 458 these times.

459 Fig. 4 shows the solutions of the homogeneous advection test after
 460 transport over $300dx$ and $30000dx$. The initial value of $h(x)$ is defined as:

$$h(i) = 4 \cdot \exp \left[- \left(\frac{x_i - x_{150}}{8} dx \right)^2 \right], \text{ for } i = 0, 1, 2, 3, \dots \quad (26)$$

461 The results for SE2, o2o3 and SE3 are shown in the left, middle and right
 462 columns of Fig. 4, respectively. At 300 time steps, the results for the three
 463 schemes are similar except for a slight oscillation in SE2. At the 30000th
 464 timestep, SE3 and o2o3 show a better simulation quality than SE2 because
 465 SE2 is only of the second order. The small difference in the accuracy between

466 o2o3 and SE3 is in accordance with the results of the numerical dispersion
 467 analysis in Section 5.3. For an analysis of the order of approximation, see
 468 Section 5.2.

Fig. 4

469 For the regular resolution case and periodic boundary conditions, both
 470 classic o4 and o2o3 are conserved. However, a lack of conservation will be
 471 observed only for o4 on irregular grids in practical tests. Hence, an irregular
 472 resolution is introduced:

$$dx = \begin{cases} 1, & \text{for } i = 1, 2, \dots, 180, 211, 212, \dots, 600, \\ 2, & \text{for } i = 181, 182, \dots, 210. \end{cases} \quad (27)$$

473 For o2o3, the weights w_i occurring in Eq. (12) are given in Tab. 2. The
 474 values of the weights gradually change near $i = 180$ (Lines 3-5 compared
 475 to Line 2 in Tab. 2) and 210 (Lines 7-9 compared to Line 10 in Tab. 2).
 476 All points x_i , where $i \neq 179, 180, 181, 209, 210, 211$ according to Eq. (27),
 477 have constant $w_i^{i'} (i' = -1, -\frac{1}{2}, 0, \frac{1}{2}, 1)$ in Eq. (12), meaning that w does not
 478 depend on i . Fig. 5 shows the temporal evolution of the solution between
 479 $t = 0$ and $t = 400$. For the initial values, the peak solution is used where only
 480 one principal point ($x_{150} = 4$) is different from 0. The computational modes
 481 of both classic and weighted o4 are stronger than that of o2o3, particularly
 482 for the case of an irregular grid. Considering Steppeler et al. (2008) and
 483 Steppeler et al. (2019a), it may be assumed that the difference is due to

484 the different orders of approximation at these points, where the resolution
 485 is irregular. Classic o4 decreases to the first order at such points. This
 486 is consistent with the fact that SE schemes are suitable for an irregular
 487 resolution, which (for this simple case) also applies to o2o3.

Fig. 5

488 Mass diagrams of the solutions, defined as $\int_{\Omega} h(x)dx$, are shown in Fig.
 489 6. The formula for computing the mass is given in Eq. (13). o2o3 conserves
 490 the mass down to the round-off error, while o4 conserves the mass until the
 491 resolution jump is reached. Then, the deviation from conservation is rather
 492 strong (reaching 50%) and diminishes for advection in the coarse-resolution
 493 area.

Fig. 6

494 5.2 *Comparison of the convergence of o2o3 with that of o3o3* 495 *and SE*

496 This section investigates the approximation order of the schemes con-
 497 sidered in this paper. Because a general function can be approximated by a
 498 Fourier transformation of the sum of trigonometric functions, we investigate
 499 the accuracy of the approximation of the derivative of a cosine function $g(x)$
 500 that can be expressed as:

$$g(x) = \cos(2\pi x), \text{ for } x \in (0, 1). \quad (28)$$

501 We assume a grid distribution as follows:

$$x_i = idx(1 + \delta r_i), \text{ for } i = 0, 1, \dots, i_e, \quad (29)$$

502 where r_i is a fixed random number between zero and one. When the grid
 503 is regular we set $\delta = 0$. When the grid is irregular, δ is any positive real
 504 number between zero and one. For $\delta > 0.0$, we obtain the irregular case, and
 505 in this case, we set $\delta = 1.0$. Using the grid point values $g_i = g(x_i)$ and using
 506 the grid approximations described in Sections 3–4, the approximations $g_{x,i}^{app}$
 507 at x_i can be obtained. The corresponding exact values $g_{x,i} = -2\pi \cdot \sin(2\pi x_i)$
 508 can be used to find the approximation error as:

$$E(dx) = \max_i |g_{x,i} - g_{x,i}^{app}|. \quad (30)$$

509 Fig. 7 shows the numerical errors of its spatial derivative with $dx =$
 510 $\frac{1}{8}, \frac{1}{4}, \frac{1}{2}, 1, 2, 4, 8, 16, 32,$ and 64. The classic o4 scheme converges to the fourth
 511 order only on regular grids. For comparison, the result for SE2 on regular
 512 grids is shown to exhibit second-order convergence, meaning that there is
 513 no superconvergence for SE2. In contrast, the high-order flux computations
 514 with o2o3 lead to superconvergence.

515 Next, the convergence on an irregular grid is investigated. The grid is
 516 defined in Eq. (29) where $\delta = 1.0$. o2o3 converges to the fourth order
 517 with an irregular grid. The use of weighted o4 to compute the differences
 518 on principal grids is essential. On the other hand, the classic o4 scheme is

519 reduced to the first order for the irregular grid.

Fig. 7

520 5.3 Dispersion analysis of o2o3

521 To derive the numerical dispersion relation for o2o3, we use spectral
522 solutions following Ullrich et al. (2018). The field h is assumed to be:

$$h_j = h_0 e^{Ik(j \cdot dx - ct)}, \text{ for } j = 0, 1, 2, \dots, \quad (31)$$

523 where $I = \sqrt{-1}$ and c and k are the phase velocity and nondimensional
524 wavenumber, respectively. Then, we define the amplitudes $\vec{A} = (h_j, h_{xx,j})$
525 in the spectral space. For each k , the linear relation between \vec{A}_k and $\vec{A}_{t,k}$
526 for Eq. (1) is given by:

$$\vec{A}_{t,k} = M^k \vec{A}_k, \quad (32)$$

527 where $\vec{A}_{t,k}$ is the temporal derivative of \vec{A}_k and the matrix M^k depends on
528 the wavenumber k . The exact solution should be linearly dependent on k
529 due to:

$$\frac{\partial h_j}{\partial x_j} = Ik \cdot h_j, \quad (33)$$

530 where $x_j = j \cdot dx$ and $j = 0, 1, 2, \dots$

531 We assume that a_1^k and a_2^k are defined as the eigenvalues of the ma-
532 trix M^k . Therefore, the imaginary components of a_1^k and a_2^k represent the

533 frequency $\omega(k)$ of the wavenumber k , while the real components are the
 534 diffusivity. The phase velocity of the wavenumber k becomes $c(k) = \frac{\omega(k)}{k}$.

535 The evolution matrix M^k is given by:

$$M^k = M^1 \cdot e^{-I\delta} + M^2 + M^3 \cdot e^{I\delta} + M^4 \cdot e^{2I\delta}, \quad (34)$$

536 where M^k is applied to the amplitudes $\vec{A} = (h_j, h_{xx,j})$ and $\delta = \frac{k}{1000} \cdot 2\pi$, $k =$
 537 $0, 1, 2, \dots, 1000$. The matrices M^1, M^2, M^3, M^4 are 2×2 matrices that are
 538 given by:

$$M^1 = \begin{pmatrix} -\frac{u_0}{12dx} + \frac{2u_0}{3dx} \left(\frac{1}{2}\right) & \frac{2u_0}{3dx} \left(-\frac{dx^2}{2}\right) \\ \frac{3}{2dx^2} M_{1,1}^1 & \frac{3}{2dx^2} M_{1,2}^1 \end{pmatrix} = \begin{pmatrix} \frac{1}{4} & -\frac{1}{3} \\ \frac{3}{8} & -\frac{1}{2} \end{pmatrix} \quad (35)$$

$$M^2 = \begin{pmatrix} \frac{2u_0}{3dx} \left(\frac{1}{2}\right) - \frac{2u_0}{3dx} \left(\frac{1}{2}\right) & -\frac{2u_0}{3dx} \left(-\frac{dx^2}{2}\right) \\ -\frac{3u_0}{2dx^3} + \frac{3}{2dx^2} (M_{1,1}^2 + M_{1,1}^1) & \frac{3}{2dx^2} (M_{1,2}^2 + M_{1,2}^1) \end{pmatrix} = \begin{pmatrix} 0 & \frac{1}{3} \\ -\frac{9}{8} & 0 \end{pmatrix} \quad (36)$$

$$M^3 = \begin{pmatrix} -\frac{1}{4} & 0 \\ \frac{3u_0}{2dx^3} + \frac{3}{2dx^2} (M_{1,1}^3 + M_{1,1}^2) & \frac{3}{2dx^2} M_{1,2}^2 \end{pmatrix} = \begin{pmatrix} -\frac{1}{4} & 0 \\ \frac{9}{8} & \frac{1}{2} \end{pmatrix} \quad (37)$$

$$M^4 = \begin{pmatrix} 0 & 0 \\ \frac{3}{2dx^2} M_{1,1}^3 & 0 \end{pmatrix} = \begin{pmatrix} 0 & 0 \\ -\frac{3}{8} & 0 \end{pmatrix} \quad (38)$$

539 where M_{j_1, j_2}^k is the element of matrix M^k in row j_1 and column j_2 (we
 540 assume $dx = 1$ and $u_0 = 1$ for simplification).

541 For o2o3, Figs. 8 (a) and (b) show the phase velocity and the devia-
 542 tion of the amplification factor from unity, respectively, as functions of the
 543 nondimensional wavenumber. For comparison, the corresponding results for
 544 SE3 and o3o3 are also given. In Fig. 8 (a), we focus on the maximum of
 545 the frequency curve because the corresponding wavelength is the resolution
 546 limit for each scheme. For o2o3 and SE3, the approximated phase veloc-
 547 ities are accurate for wavelengths greater than $3dx$, with o3o3 performing
 548 somewhat worse. For smaller wavelengths, the derivative of the frequency
 549 curve becomes negative, resulting in a negative group velocity. This means
 550 that for this range of wavenumbers, the solution is not useful in terms of the
 551 propagation of wave packets. Based on this criterion, the useful wavelength
 552 range for o2o3 is larger than that for o3o3 by approximately dx . Finally, as
 553 shown in Fig. 8 (b), the amplification factor is one for all three schemes,
 554 and thus, the schemes are all nondiffusive.

Fig. 8

555 The part of the spectrum with negative group velocities should be fil-
 556 tered. Sometimes, a more elaborate definition of the essential resolution is
 557 used (Ullrich 2014). This is based on the realistically approximated part
 558 of the dispersion diagram that shows the frequency as a function of the
 559 wavenumber. We note that o2o3 does not have the large 0-space of o3o3.
 560 The 0-space is a space where waves are stationary for a relatively large num-
 561 ber of wavenumber values. For o3o3, there exists a 0-space with wavenum-

562 ber values where physical waves are not captured (Steppeler et al. 2019a).
563 Thus, o2o3 is simpler to execute than o3o3.

564 Although SE3 has a marginally larger useful wavelength range than o2o3,
565 we note that the dispersion relation for SE3 shows a spectral gap, as indi-
566 cated by black circles in Fig. 8 (a). A spectral gap is a small wiggle on the
567 frequency curve leading to a small area of negative group velocities in an
568 otherwise well-resolved k -area located around the wavelength $8dx$ in Fig. 8
569 (a). Due to this spectral gap of SE3, Steppeler et al. (2019a) concluded that
570 o3o3 has performance advantages over SE3. In contrast, o2o3 and o3o3 do
571 not have spectral gaps. The methods for reducing the effect of the spectral
572 gap for SE3 by applying hyperdiffusion have been discussed in the literature
573 (Ullrich et al. 2018). In the absence of a spectral gap, an estimate of the
574 usefully resolved wavenumber k is the range of k up to the maximum.

575 5.4 Von Neumann stability analysis of o2o3 for finite dt

576 In this section, the 1D advection equation in Eq. (1) is used for the
577 classic Von Neumann stability analysis of o2o3. The waveform solution Eq.
578 (31) of the field h and the linear relation Eq. (32) between \vec{A}_k and $\vec{A}_{t,k}$ are
579 utilized for this analysis.

580 For RK4 time integration, the amplification factor G is given by:

$$G = E + \frac{1}{6}(M^k + 2 \cdot M_{RK2}^k + 2 \cdot M_{RK3}^k + M_{RK4}^k)dt, \quad (39)$$

581 where E is the identity matrix and

$$\begin{cases} M_{RK2}^k = M^k (E + \frac{1}{2}M^k dt), \\ M_{RK3}^k = M^k (E + \frac{1}{2}M_{RK2}^k dt), \\ M_{RK4}^k = M^k (E + M_{RK3}^k dt). \end{cases} \quad (40)$$

582 The amplification factor G for o2o3 is shown in Fig. 9. The resulting
 583 stability is achieved for CFL = 1.9, consistent with the values obtained in
 584 Section 5.1.

Fig. 9

585 5.5 2D cut-cell results using a sparse grid

586 As stated in Section 2, o2o3 can be easily adapted for 2D advection
 587 over simple terrain. This method is completely analogous to the method in
 588 Steppeler et al. (2019a) and can be considered a generalization of the o1o1
 589 scheme treated by Steppeler and Klemp (2017). For details regarding the
 590 calculation, the readers are referred to Steppeler et al. (2019a). Here, we
 591 give only a short description.

592 Following Steppeler and Klemp (2017), we conduct a 2D advection test
 593 along the profile of a mountain composed of a straight line oriented at an
 594 angle of 45 degrees. This test problem is very simple; we assume that the

595 velocity is parallel to this straight line, and the velocity components (u_0
596 and w_0) are constant (1, 1). Despite the extreme simplicity of this example,
597 Steppeler and Klemp (2017) showed that noise can be generated along the
598 orographic line. We can examine how this kind of noise can be avoided.

599 Fig. 10 shows that the sparse grid is available in the same manner as for
600 o3o3. However, there is a difference in the sparseness factor between o2o3
601 and o3o3. The sparseness factor is the ratio of the number of grid points
602 in the sparse grid to that in the full grid. According to Steppeler et al.
603 (2019a), o3o3 has a sparseness factor of $\frac{5}{9}$, whereas o2o3 has a sparseness
604 factor of $\frac{3}{4}$ (as illustrated in Fig. 2). Comparing the result of Fig. 10 with
605 that of Steppeler et al. (2019a) with a sparse grid, we find that o2o3 has
606 fewer unused points than o3o3. However, discussing this finding in terms
607 of practical modelling and numerical computation reduction is beyond the
608 scope of this paper.

Fig. 10

609 We define the fluxes in the x - and z -directions as follows:

$$\begin{cases} Fl^x = u \cdot h(x, z), \\ Fl^z = w \cdot h(x, z). \end{cases} \quad (41)$$

610 The flux divergences in the x - and z -directions at the principal points are
611 computed by classic o4 because the cut and uncut cells in this case are
612 regular. However, Eq. (12) must not be invoked because it is suitable for

613 irregular grids. Applying the principle of mass conservation according to
 614 Steppeler et al. (2019a) and the formula obtained in Section 3, we obtain:

$$Fl_{x,i+\frac{1}{2},k}^x = \frac{3}{2} \frac{Fl_{i+1,k}^x - Fl_{i,k}^x}{dx} - \frac{1}{2} \frac{Fl_{x,i+1,k}^x + Fl_{x,i,k}^x}{2}. \quad (42)$$

615 For $Fl_{z,i,k+\frac{1}{2}}^x$, the result is similar. For the divergence in the z -direction, the
 616 same procedure is followed using the z -coordinate lines. The spectral am-
 617 plitudes $Fl_{xx,i+\frac{1}{2},k}$ and $Fl_{zz,i,k+\frac{1}{2}}$ are then uniquely determined by requiring
 618 mass conservation for the fluxes in the x - and z -directions, respectively.

619 For uncut cells, this procedure is straightforward and analogous to o3o3.
 620 For the cut cells, a coordinate along the surface line is introduced. For
 621 this specific test problem, the streamlines of advection are parallel to the
 622 surface line $x = z$ such that there is no flux and no flux divergence in the
 623 direction perpendicular to the surface. Because the orography is diagonal
 624 to the model area, the principal points lie on the orographic line that can
 625 be treated by classic o4. No interpolation is necessary for orography to cut
 626 the cells diagonally.

627 To this line $x = z$, we assume a coordinate s in the diagonal line with
 628 $ds = \sqrt{2}dx$. Therefore, Eq. (42) for s -axis takes the form:

$$Fl_{s,i+\frac{1}{2},k+\frac{1}{2}}^s = \frac{3}{2} \frac{Fl_{i+1,k+1}^s - Fl_{i,k}^s}{ds} - \frac{1}{2} \frac{Fl_{x,i+1,k+1}^s + Fl_{x,i,k}^s}{2}, \quad (43)$$

629 in which $Fl_{i,k}^s = \sqrt{2}Fl_{i,k}^x$ because the flux is in the direction of the di-

630 agonal line. In addition, the time derivatives for the principal points on
631 the boundary are obtained by differentiating along the diagonal boundary.
632 Rather than rectangles, cut-cell grids can be applied for rhombohedral grids,
633 resulting in quadrilaterals with two angles not equal to $\frac{\pi}{2}$. This will com-
634 plicate the computation of mass contributions by the different amplitudes
635 relative to the rectangular grid case used here. However, in more general
636 cases, the principle of mass conservation is used in the same manner as with
637 squares to determine the amplitudes of the time derivatives at the midpoints
638 of the edges.

639 For the experimental setup, we use a square grid of 140×140 grid points
640 with $dx = dz = 1.0$, and we perform temporal integration for 100 time steps
641 with $dt = 1.0$. The results for o2o3 are shown in Fig. 10 and can be com-
642 pared directly to those by Steppler and Klemp (2017). The inaccuracies
643 and noise for this problem, as seen for some non-Galerkin treatments, are
644 absent; o2o3 is able to advect a structure along a straight line without gen-
645 erating noise. This result is consistent with that for the first-order Galerkin
646 approach and with that obtained by Savre et al. (2016), who reported fewer
647 numerical boundary-related errors for the classic Galerkin method. These
648 results indicate that cut cells may be applicable with polynomial represen-
649 tations higher than one.

650 The cut-cell example shown above is a rather special case because it is

651 valid only when the orography passes through the diagonal of cells. The
652 more general case where the orography is any straight line can be treated
653 with only little more effort. The computational domain consists of the points
654 above the orography. As the orography is a straight line of direction (u_0, u_0) ,
655 we define the flux as (u_0h, u_0h) where h is the density. This means that the
656 flux has no component perpendicular to the orography at each point on the
657 orography. We call this the pointwise boundary scheme. Another option
658 not followed in this paper would be to use the less stringent condition that
659 the integrals of the vertical flux components over segments of the orographic
660 line are zero.

661 The orography for the general case is shown in Fig. 11 (b) as a green
662 line. The nondiagonal computational domain above the green line (gray
663 area in Fig. 11b) is notated as S_{nd} , while the diagonal domain above the
664 red line (gray area in Fig. 11a) is correspondingly notated as S_d . Near the
665 nondiagonal boundary, we have cells with triangles or pentagons marked in
666 green, while the cells are squares and triangles at the diagonal boundary
667 in red. There is more than one way to define the field representations near
668 the small boundary sections in triangles/pentagons, and we are seeking the
669 simplest scheme. Note that a polynomial function defined in a part of a
670 rectangular cell, such as the small cut-cell triangles/pentagons in Fig. 11
671 (b), can be uniquely extended to the whole cell. Therefore, it is possible

672 to define fields in the area S_{nd} by adopting the same discretization (such as
673 Eq. (43)) in the larger area S_d and restrict the field values in S_{nd} . Thus,
674 we can further define the temporal scheme in S_{nd} to be the same as that in
675 S_d because S_d and S_{nd} share the common area S_{nd} .

676 Let us assume the mass M_S for the area S :

$$M_S(t) = \iint_S h(x, z) dx dz, \quad (44)$$

677 in which S can be either S_d or S_{nd} . When we define the S_{nd} scheme to
678 be the restriction of the S_d scheme to the smaller area, we must show that
679 a closed system is obtained. This means that no mass is lost through the
680 boundary of S_{nd} , indicating that the fluxes of the S_d scheme are parallel to
681 the boundary of S_{nd} (green line in Fig. 11) and to the boundary of S_d (red
682 dotted line in Fig. 11). We can apply Stokes theorem to Eq. (1). For the
683 time derivative of $M_{S_{nd}}$ we obtain:

$$\frac{\partial M_{S_{nd}}}{\partial t} = \iint_{S_{nd}} h_t dx dz = \int_{\partial S_{nd}} Fl^\perp(l) dl = 0, \quad (45)$$

684 in which Fl^\perp is the flux component orthogonal to the boundary of S_{nd} in
685 Fig. 11 (b). Thus, according to the scheme adopted in the area S_d , the mass
686 is also conserved in S_{nd} due to the absence of flux components perpendicular
687 to the green line. For convenience, we can define phantom amplitude points
688 for the cut cells outside the computational domain and perform FDs for the

Fig. 11

689 area above the dotted line in Fig. 11 (b).

690 The case of cut cells with a curved boundary is beyond the scope of
691 this paper. The derivations of Eqs. (44)-(45) use the pointwise cancella-
692 tion of the flux at the boundary, which follows from the assumption of a
693 constant velocity. However, the extension of fields and fluxes beyond the
694 small triangles and pentagons can also be useful for a more general orogra-
695 phy. When the orography is not a straight line but rather a linear spline
696 and the x -component of the flux is represented as a piecewise continuous
697 polynomial spline, the z -component of the flux vector must have a discon-
698 tinuous representation. It follows from that fact that a curved piecewise
699 linear spline for the orography changes direction at the corner points in
700 a discontinuous manner. Therefore, the function obtained by differentia-
701 tion would be treated as a discontinuous function. Second-order staggered
702 Arakawa C-grid schemes can be obtained as low-order LG schemes by a
703 discontinuous piecewise linear 2D spline (Steppeler 1989). This is achieved
704 by assuming constant piecewise fields for the density and representing the
705 velocity components u and w as piecewise linear splines. Specifically, u is
706 set to be continuous and piecewise linear in the x -direction and piecewise
707 constant in the z -direction. w is represented in a similar manner by swap-
708 ping the treatment to u in the x - and z -directions. The generalization
709 to orographic surfaces represented by linear splines can be accomplished by

710 generalizing the low-order Galerkin representation of Steppeler (1989) to a
711 higher polynomial order.

712 **6. Conclusion**

713 This study has investigated an alternative LG method referred to as
714 o2o3. This method represents the field h by piecewise quadratic polyno-
715 mials and the fluxes by degree-3 polynomials. o2o3 inherits not only the
716 accuracy of SE3 but also the geometric flexibility of FE methods and the
717 potentially strong scalability of SE techniques. Furthermore, o2o3 uses a
718 regular collocation grid and allows a larger time step than SE3. The al-
719 lowed time step is the same as that of standard fourth-order differencing.
720 The transition to the LG approach is an advance compared to conventional
721 fourth-order differencing, as the proposed method is mass conserving, and a
722 conservation law may be achieved for each equation used in a multi-equation
723 system.

724 **Acknowledgements**

725 No author reported any potential conflicts of interest. This research
726 was made possible by a research visit of all authors in Bad Orb, Germany,
727 financed by the National Natural Science Foundation of China (Grant No.

728 41905093), the China Scholarship Council (No. 201904910136), and the UK
729 EPSRC Project (MAGIC, Grant No. EP/N010221/1). The authors thank
730 the city of Bad Orb for the support of the visit by providing office space.
731 To discuss these results, the Mathematics workshop of Weather 2019, 14-16
732 October in Bad Orb, was organized by the first author in cooperation with
733 the Freie Universität Berlin and Imperial College London. The conference
734 was supported by the German Research Council (DFG, Grant No. KL
735 611/26-1) and the Hessian Ministerium für Wissenschaft und Kunst.

736

References

- 737 Ahlberg, J. H., E. N. Nilson, and Walsh, 1967: *The theory of splines and*
738 *their application*. Academic Press New York, 535 pp.
- 739 Durran, D., 2010: Numerical methods for fluid dynamics: With applications
740 to geophysics, 2nd edn. *Springer*.
- 741 Giraldo, F. X., 2001: A spectral element shallow water model on spherical
742 geodesic grids. *Num. Meth. Fluids*, **8**, 869–901.
- 743 Giraldo, F. X., and T. E. Rosmond, 2004: A scalable spectral element
744 eulerian atmospheric model (SEE-AM) for NWP: dynamical core
745 tests. *Mon. Wea. Rev.*, **132(1)**, 133–153.

746 Herrington, A. R., P. H. Lauritzen, M. A. Taylor, S. Goldhaber, B. E. Eaton,
747 K. A. Reed, and P. A. Ullrich, 2019: Physics-dynamics coupling
748 with element-based high-order Galerkin methods: Quasi equal-area
749 physics grid. *Mon. Wea. Rev.*, **147**, 69–84.

750 Kelly, J. F., and F. X. Giraldo, 2012: Continuous and discontinuous
751 Galerkin methods for a scalable three-dimensional nonhydrostatic at-
752 mospheric model: limited-area mode. *J. Comput. Phys.*, **231**, 7988–
753 8008.

754 Marras, S., J. F. Kelly, M. Moragues, A. Muller, M. A. Kopera, M. Vazquez,
755 F. X. Giraldo, G. Houzeaux, and O. Jorba, 2016: A review of
756 element-based Galerkin methods for numerical weather prediction:
757 Finite element, spectral elements, and discontinuous Galerkin. *Arch.*
758 *Computat. Methods Eng.*, **23**, 673–722.

759 Nishikawa, Y., and M. Satoh, 2016: A conserved topographical representa-
760 tion scheme using a thin-wall approximation in z-coordinates. *SOLA*,
761 **12**, 232–236.

762 Phillips, N. A., 1957: A coordinate system having some special advantages
763 for numerical forecasting. *J. Meteor.*, **14**, 184–185.

764 Savre, J., J. Percival, M. Herzog, and C. C. Pain, 2016: Two-
765 dimensionanl evaluation of ATHAM-Fluidity, a nonhydrostatic atmo-

766 spheric model using mixed continuous/discontinuous finite elements
767 and anisotropic grid optimization. *Mon. Wea. Rev.*, **144**, 4349–4372.

768 Simmons, A. J., D. M. Burridge, M. Jarraud, C. Girard, and W. Wergen,
769 1989: The ecmwf medium-range prediction models development of
770 the numerical formulations and the impact of increased resolution.
771 *Meteorol. Atmos. Phys.*, **40**, 28–60.

772 Skamarock, W. C., J. B. Klemp, M. G. Duda, L. D. Fowler, S. H. Park, and
773 T. Ringler, 2012: A multiscale nonhydrostatic atmospheric model
774 using centroidal Voronoi tessellations and C-grid staggering. *Mon.*
775 *Wea. Rev.*, **140**, 3090–3105.

776 Steppeler, J., 1987: *Galerkin and finite element methods in numerical*
777 *weather prediction*. Duemmler Bonn, 535 pp.

778 Steppeler, J., 1989: Analysis of group velocities of various finite element
779 schemes. *Beitr. Phys. Atmos.*, **62**, 151–161.

780 Steppeler, J., H. W. Bitzer, Z. Janjic, U. Schättler, P. Prohl, U. Gjertsen,
781 L. Torrisi, J. Parfinievicz, E. Avgoustoglou, and U. Damrath, 2006:
782 Prediction of clouds and rain using a z-coordinate nonhydrostatic
783 model. *Mon. Wea. Rev.*, **134**, 3625–3643.

784 Steppeler, J., G. Doms, U. Schättler, H. W. Bitzer, A. Gassmann, U. Dam-

785 rath, and G. Gregoric, 2003: Meso Gamma scale forecasts using the
786 nonhydrostatic model LM. *Meteorol. Atmos. Phys.*, **182**, 75–96.

787 Steppeler, J., and J. B. Klemp, 2017: Advection on cut-cell grids for an
788 idealized mountain of constant slope. *Mon. Wea. Rev.*, **145**, 1765–
789 1777.

790 Steppeler, J., J. Li, F. Fang, J. Zhu, and P. A. Ullrich, 2019a: a
791 variant of spectral elements with a regular collocation grid. *Mon.*
792 *Wea. Rev.*, **147**, 2067–2082.

793 Steppeler, J., J. Li, I. M. Navon, F. Fang, and Z. Xiao, 2019b: Medium
794 range forecasts using cut-cells: a sensitivity study. *Meteorol. Atmos.*
795 *Phys.*, **8**, 4349–4372.

796 Steppeler, J., M. Navon, and H. Lu, 1990: Finite-element schemes for ex-
797 tended integrations of atmospheric models. *J. Comput. Phys.*, **89**,
798 95–124.

799 Steppeler, J., P. Ripodas, and S. Thomas, 2008: Third order finite difference
800 schemes on isocahedral-type grids on the sphere. *Mon. Wea. Rev.*,
801 **136**, 2683–2698.

802 Taylor, M., J. Tribbia, and M. Iskandarani, 1997: The spectral element

803 method for the shallow water equations on the sphere. *J. Comput.*
804 *Phys.*, **130**, 92–108.

805 Tomita, H., M. Tsugawa, M. Satoh, and K. Goto, 2001: Shallow water
806 model on a modified isosahedral geodesic grid by using spring dy-
807 namics. *J. Comput. Phys.*, **174**, 579–613.

808 Ullrich, P. A., 2014: Understanding the treatment of waves in atmospheric
809 models. Part I: The shortest resolved waves of the 1D linearized
810 shallow-water equations. *Quart. J. Roy. Met. Soc.*, **140**, 1426–1440.

811 Ullrich, P. A., D. R. Reynolds, J. E. Guerra, and M. A. Taylor, 2018:
812 Impacts and importance of diffusion on the spectral element method:
813 A linear analysis. *J. Comput. Phys.*, **375**, 427–446.

814 Yamazaki, H., and T. Satomura, 2010: Nonhydrostatic atmospheric mod-
815 eling using a combined Cartesian grid. *Mon. Wea. Rev.*, **132**, 3932–
816 3945.

817 Yamazaki, H., T. Satomura, and N. Nikiforakis, 2016: Three-dimensional
818 cut-cell modelling for high-resolution atmospheric simulations.
819 *Quart. J. Roy. Met. Soc.*, **142**, 1335–1350.

820 Zängl, G., 2012: Extending the numerical stability limit of terrain-following
821 coordinate models over steep slopes. *Mon. Wea. Rev.*, **140**, 37223733.

List of Figures

823	1	Grids for o2o3, SE2 and SE3, in which the solid black points represent the principal nodes and the dashed white points represent the interior nodes of the elements.	50
824			
825			
826	2	o2o3 computational grid in two dimensions: (a) full grid and (b) sparse grid where unused points are shown in white. . . .	51
827			
828	3	Approximations of the flux and the flux derivative of the field $h(x)$ by the (a) SE2, (b) o2o3 and (c) SE3 schemes. The solid curves are the field $h(x)$, and the dashed curves are the flux. The dotted curves represent the derivative of the flux, while the blue curves represent the regularized derivative, which is the derivative approximated by a continuous function. The regularized derivative is applied with SE2 and SE3. The grid intervals are shown corresponding to the dotted curves, where the long vertical lines represent the principal points and the short vertical lines are the interior points. In (a) and (c), the flux is different from $h(x)$ only by the factor -1 . In (b), the flux $fl(x)$ is approximated by a differentiable function, and the flux derivative does not need to be regularized, as $fl(x)$ is differentiable. In (c), $h(x)$ is a third-order representation.	52
829			
830			
831			
832			
833			
834			
835			
836			
837			
838			
839			
840			
841			
842	4	Solutions of the homogeneous advection equation with periodic boundary conditions after transport over $300dx$ and $30000dx$, and the length of the horizontal area is $600dx$. The initial condition centered at $150dx$ is shown in (a). The second row shows the results after transport over $300dx$, while the third row shows the results after transport over $30000dx$. The left, middle and right columns are the results with SE2, o2o3 and SE3, respectively. Due to $dx = dt = 1$, the transport of $30000dx$ is done in $30000dt$. This value of dt means that all schemes perform well in their CFL limit.	53
843			
844			
845			
846			
847			
848			
849			
850			
851			

852	5	Solution of a single cell peak for the (a) classic o4 scheme	
853		with a regular cell structure, (b) weighted o4 scheme with an	
854		irregular cell structure, (c) o2o3 scheme with a regular cell	
855		structure and (d) o2o3 scheme with an irregular cell structure.	
856		The black curves are the initial field and the forecasts	
857		at $t = 100, 200, 300,$ and $400,$ and the red and blue curves are	
858		the forecasts at $t = 30$ and $t = 60$ at the start and end of the	
859		resolution jumps.	54
860	6	Mass diagrams for the (a) classic o4 scheme with a regular	
861		cell structure, (b) weighted o4 scheme with an irregular cell	
862		structure, (c) o2o3 scheme with a regular cell structure and	
863		(d) o2o3 scheme with an irregular cell structure. With the	
864		nonconserving o4 scheme, deviations of mass conservation occur	
865		when the advected structure reaches the lower-resolution area	
866		and to a smaller degree when the highly resolved area is	
867		reached again.	55
868	7	Convergence speeds of o4, o2o3 and SE2 under irregular and	
869		regular grids for different grid spacings: $dx = \frac{1}{8}, \frac{1}{4}, \frac{1}{2}, 1, 2, 4, 8, 16, 32,$	
870		and $64.$ The left, middle and right panels are the results for	
871		o4, o2o3 and SE2, respectively. The circles represent the error	
872		norms for a regular grid, where Eq. (11) is used for o4	
873		and o2o3, while the squares represent the error norms for an	
874		irregular grid, where Eq. (11) is used for o4, and the rhom-	
875		buses are the error norms for an irregular grid, where Eq.	
876		(12) is used for o4 and o2o3. The squares in the left panel	
877		are used for classic o4 according to Eq. (11), leading to a	
878		first-order scheme on an irregular grid.	56
879	8	Dispersion relations for o2o3, SE3, and o3o3. (a) is the imagi-	
880		nary part and (b) is the deviation of the eigenvalues from one,	
881		which is a measure of the intrinsic diffusivity of the scheme.	
882		All three schemes are non-diffusive. The black circles mark	
883		the spectral gap for SE3, producing negative group velocities	
884		in an area where the neighboring wavenumber values indicate	
885		a well-resolved solution.	57
886	9	(a) Von Neumann analysis results for o2o3. (b) is the cross-	
887		section of (a) at the nondimensional wavenumber $k = \pi.$. . .	58

888	10	2D results of o2o3 with a cut-cell grid under a straight line representing the terrain. The tracer in the first row is above the terrain, while the tracer in the second row is advected along the terrain. The first column presents the initial values of the tracers and the advection results after 100 time steps. The second column shows magnified views of the field at the locations of the initial values. The third column shows magnified views of the forecast fields. (b) and (e) show a background comprising zero field values with clusters of higher values. These points are marked in white in Fig. 2 (b); as these points are unused for forecasting, they retain their initial values. (c) and (f) show a smooth structure representing the field. At some points corresponding to the points marked in white in Fig. 2 (b), there is a steep point valley assuming the value of zero. The contour interval is set to be 0.5. . . .	59
889			
890			
891			
892			
893			
894			
895			
896			
897			
898			
899			
900			
901			
902			
903	11	Different options for the cut-cell grid. (a) Special case of a straight orographic line going through the cell corners, as was used in the example of Fig. 10. All cut cells in this case are triangular marked with red colors. (b) A general case where the orography does not cut each cell diagonally. The thick solid and green lines mark the boundary approximation cells. The cut cells are triangles or pentagons shown in green. The physical domains are the gray areas marked with S_d in (a) and S_{nd} in (b). The mass of the system is the integral of the density over the area above the orography. The polynomial field representations for the fluxes and the density can be uniquely extended to the whole area of the boundary approximation cells.	60
904			
905			
906			
907			
908			
909			
910			
911			
912			
913			
914			
915			

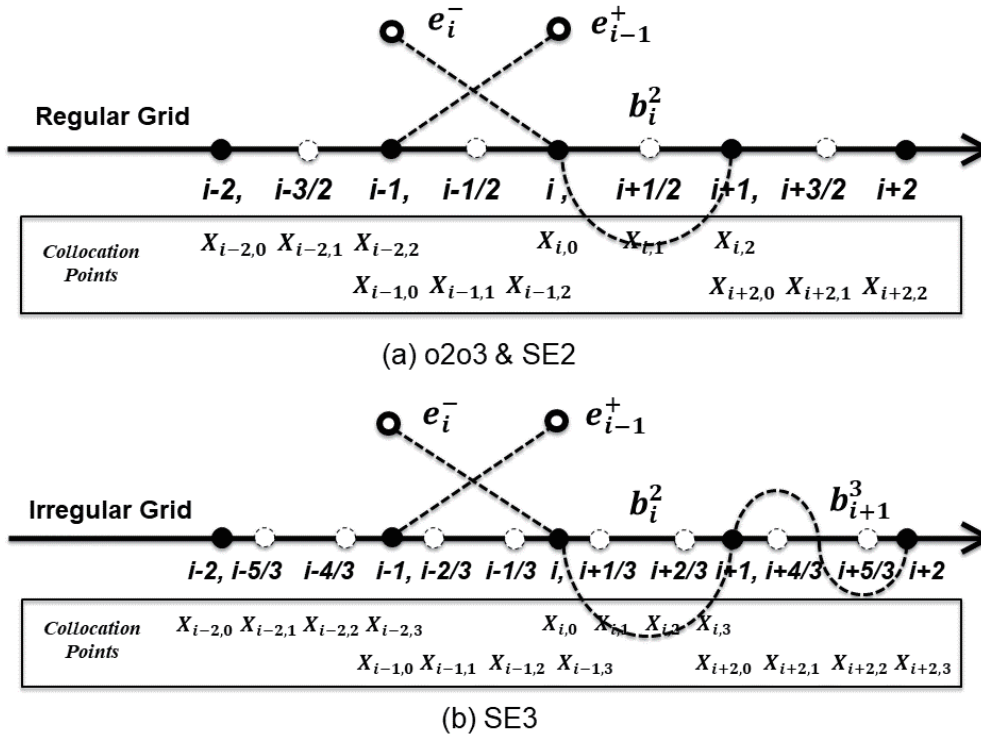


Fig. 1. Grids for o2o3, SE2 and SE3, in which the solid black points represent the principal nodes and the dashed white points represent the interior nodes of the elements.

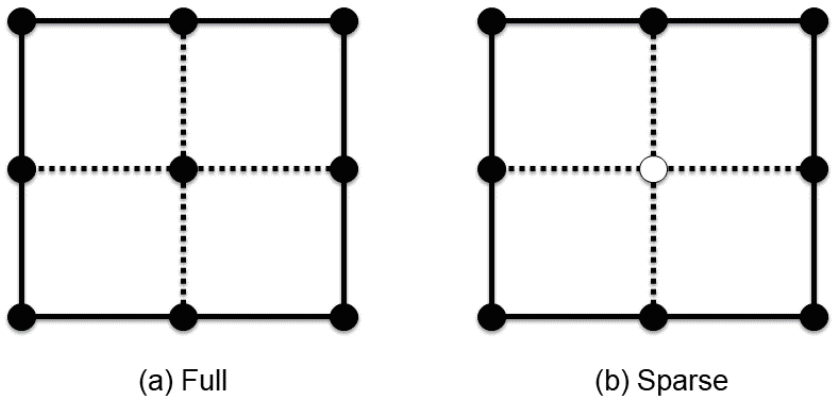


Fig. 2. o2o3 computational grid in two dimensions: (a) full grid and (b) sparse grid where unused points are shown in white.

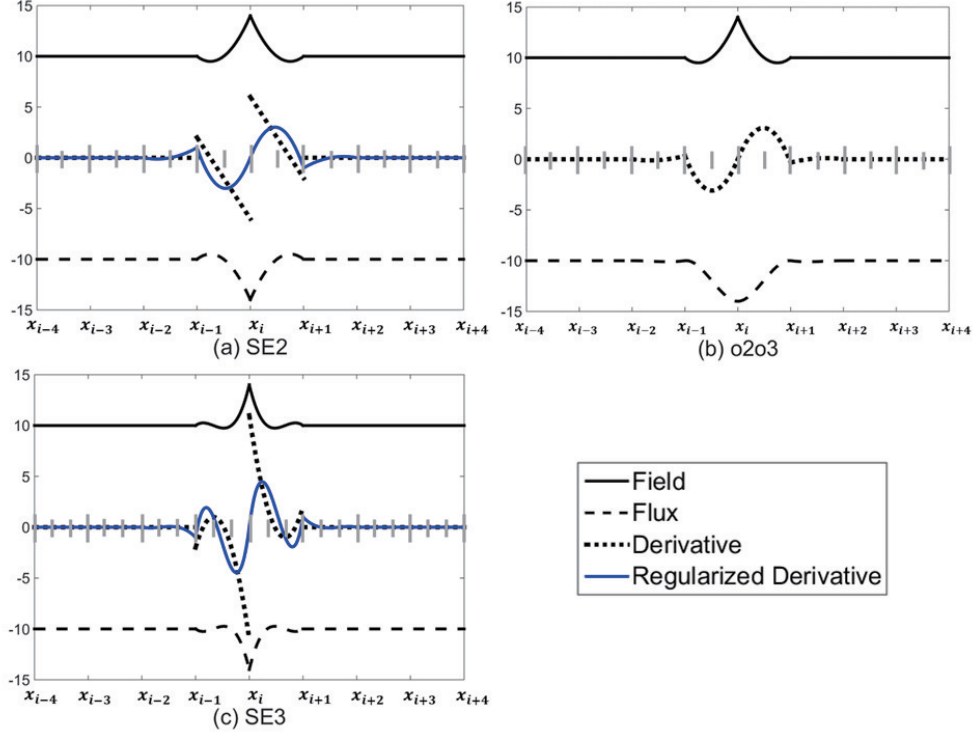


Fig. 3. Approximations of the flux and the flux derivative of the field $h(x)$ by the (a) SE2, (b) o2o3 and (c) SE3 schemes. The solid curves are the field $h(x)$, and the dashed curves are the flux. The dotted curves represent the derivative of the flux, while the blue curves represent the regularized derivative, which is the derivative approximated by a continuous function. The regularized derivative is applied with SE2 and SE3. The grid intervals are shown corresponding to the dotted curves, where the long vertical lines represent the principal points and the short vertical lines are the interior points. In (a) and (c), the flux is different from $h(x)$ only by the factor -1 . In (b), the flux $fl(x)$ is approximated by a differentiable function, and the flux derivative does not need to be regularized, as $fl(x)$ is differentiable. In (c), $h(x)$ is a third-order representation.

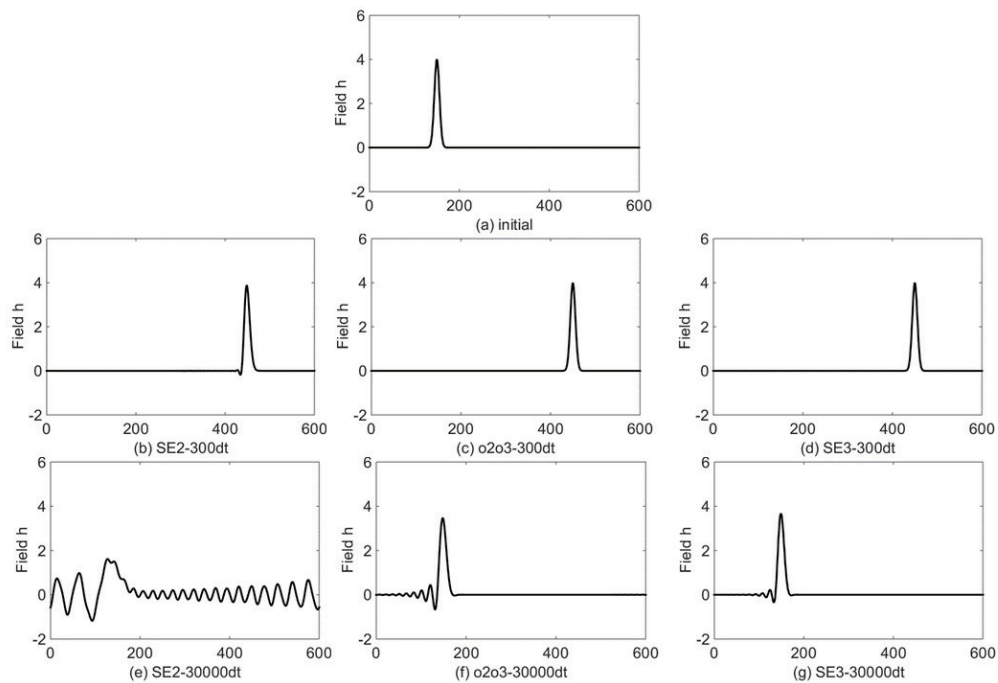


Fig. 4. Solutions of the homogeneous advection equation with periodic boundary conditions after transport over $300dx$ and $30000dx$, and the length of the horizontal area is $600dx$. The initial condition centered at $150dx$ is shown in (a). The second row shows the results after transport over $300dx$, while the third row shows the results after transport over $30000dx$. The left, middle and right columns are the results with SE2, o2o3 and SE3, respectively. Due to $dx = dt = 1$, the transport of $30000dx$ is done in $30000dt$. This value of dt means that all schemes perform well in their CFL limit.

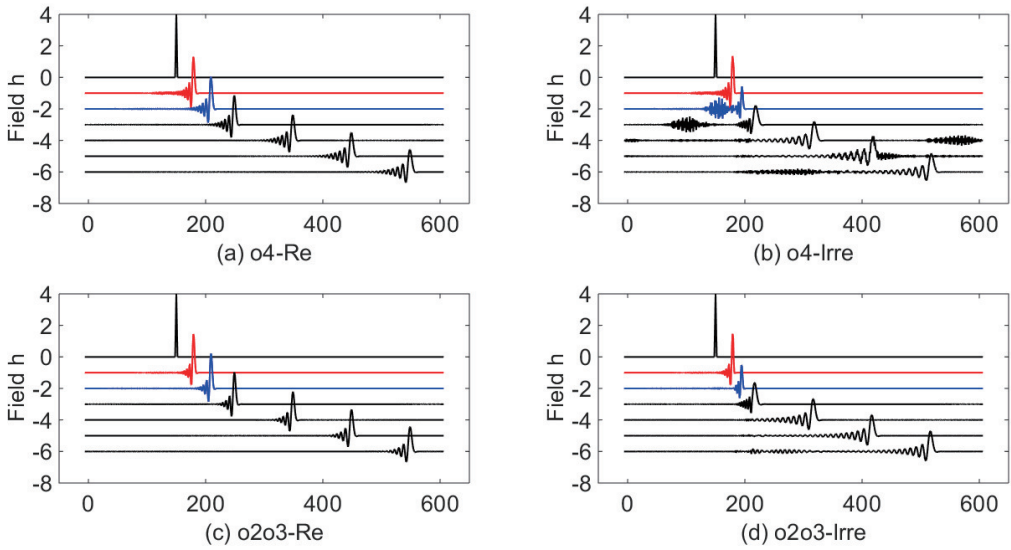


Fig. 5. Solution of a single cell peak for the (a) classic o4 scheme with a regular cell structure, (b) weighted o4 scheme with an irregular cell structure, (c) o2o3 scheme with a regular cell structure and (d) o2o3 scheme with an irregular cell structure. The black curves are the initial field and the forecasts at $t = 100, 200, 300,$ and 400 , and the red and blue curves are the forecasts at $t = 30$ and $t = 60$ at the start and end of the resolution jumps.

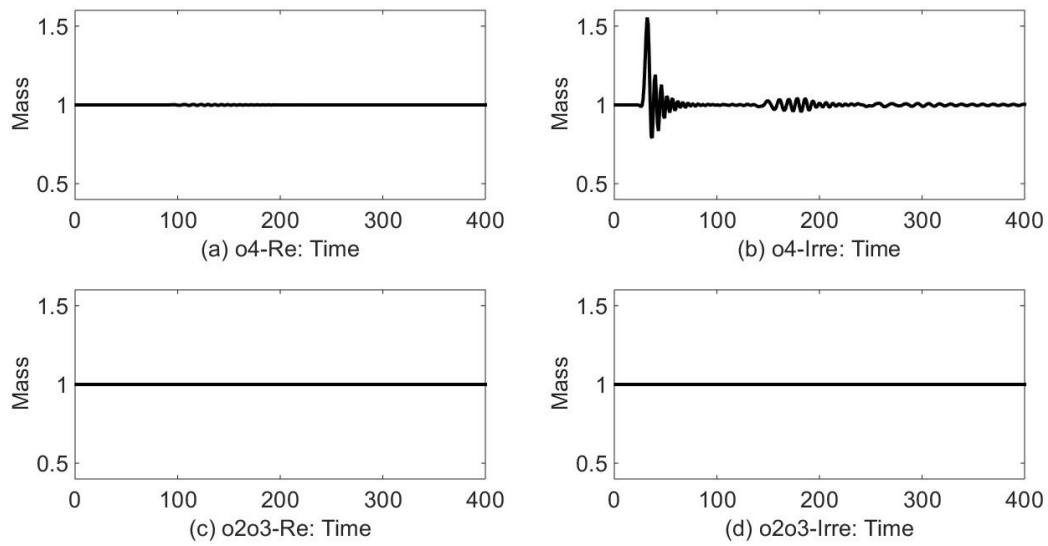


Fig. 6. Mass diagrams for the (a) classic o4 scheme with a regular cell structure, (b) weighted o4 scheme with an irregular cell structure, (c) o2o3 scheme with a regular cell structure and (d) o2o3 scheme with an irregular cell structure. With the nonconserving o4 scheme, deviations of mass conservation occur when the advected structure reaches the lower-resolution area and to a smaller degree when the highly resolved area is reached again.

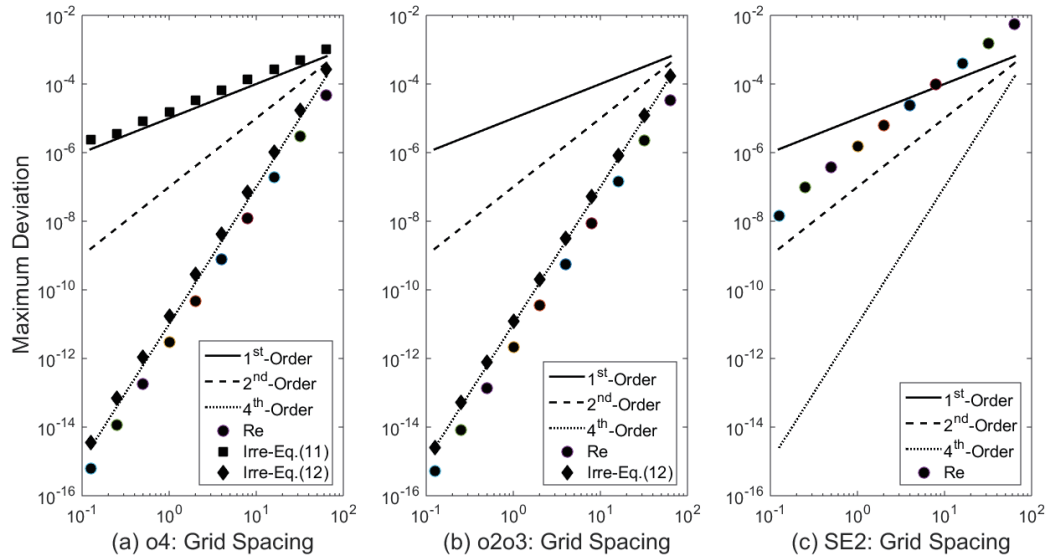


Fig. 7. Convergence speeds of o4, o2o3 and SE2 under irregular and regular grids for different grid spacings: $dx = \frac{1}{8}, \frac{1}{4}, \frac{1}{2}, 1, 2, 4, 8, 16, 32,$ and 64 . The left, middle and right panels are the results for o4, o2o3 and SE2, respectively. The circles represent the error norms for a regular grid, where Eq. (11) is used for o4 and o2o3, while the squares represent the error norms for an irregular grid, where Eq. (11) is used for o4, and the rhombuses are the error norms for an irregular grid, where Eq. (12) is used for o4 and o2o3. The squares in the left panel are used for classic o4 according to Eq. (11), leading to a first-order scheme on an irregular grid.

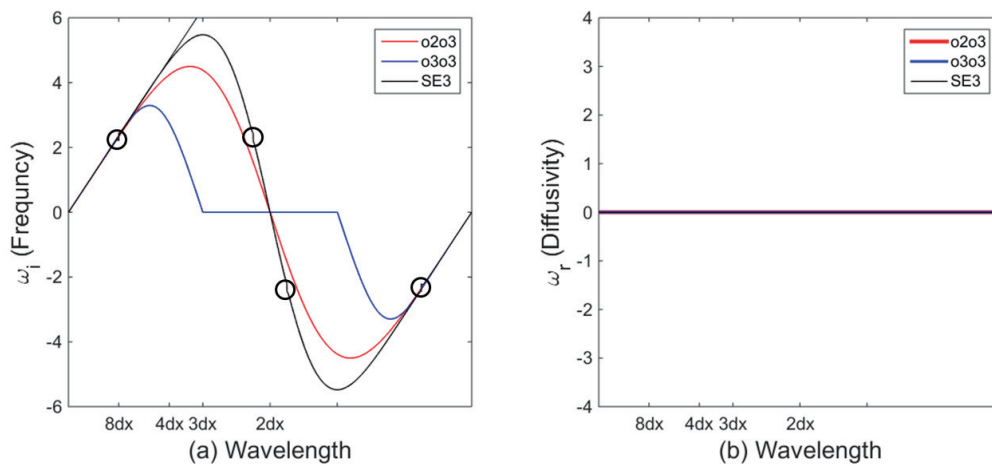


Fig. 8. Dispersion relations for o2o3, SE3, and o3o3. (a) is the imaginary part and (b) is the deviation of the eigenvalues from one, which is a measure of the intrinsic diffusivity of the scheme. All three schemes are non-diffusive. The black circles mark the spectral gap for SE3, producing negative group velocities in an area where the neighboring wavenumber values indicate a well-resolved solution.

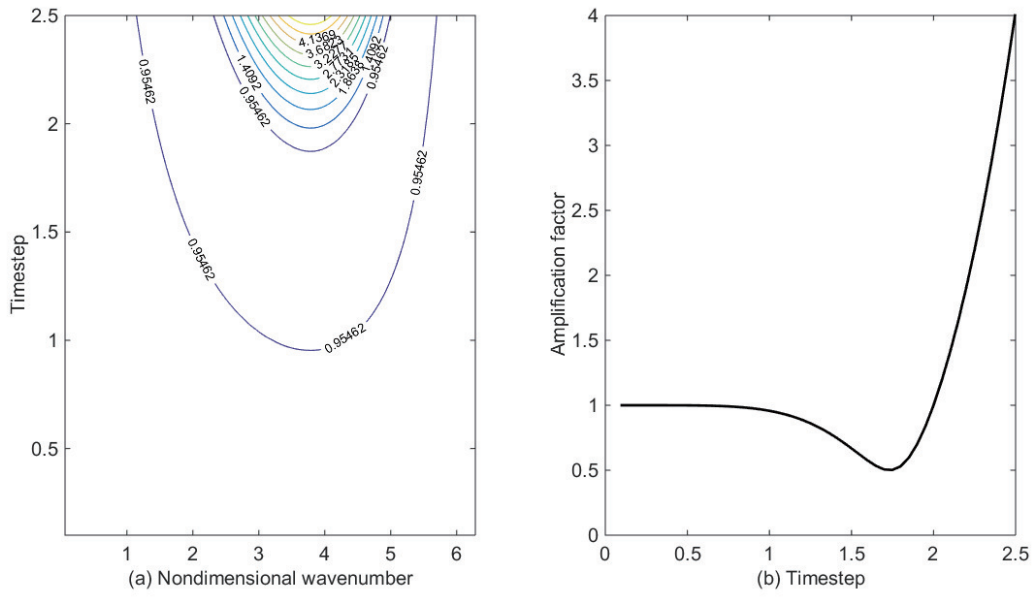


Fig. 9. (a) Von Neumann analysis results for o2o3. (b) is the cross-section of (a) at the nondimensional wavenumber $k = \pi$.

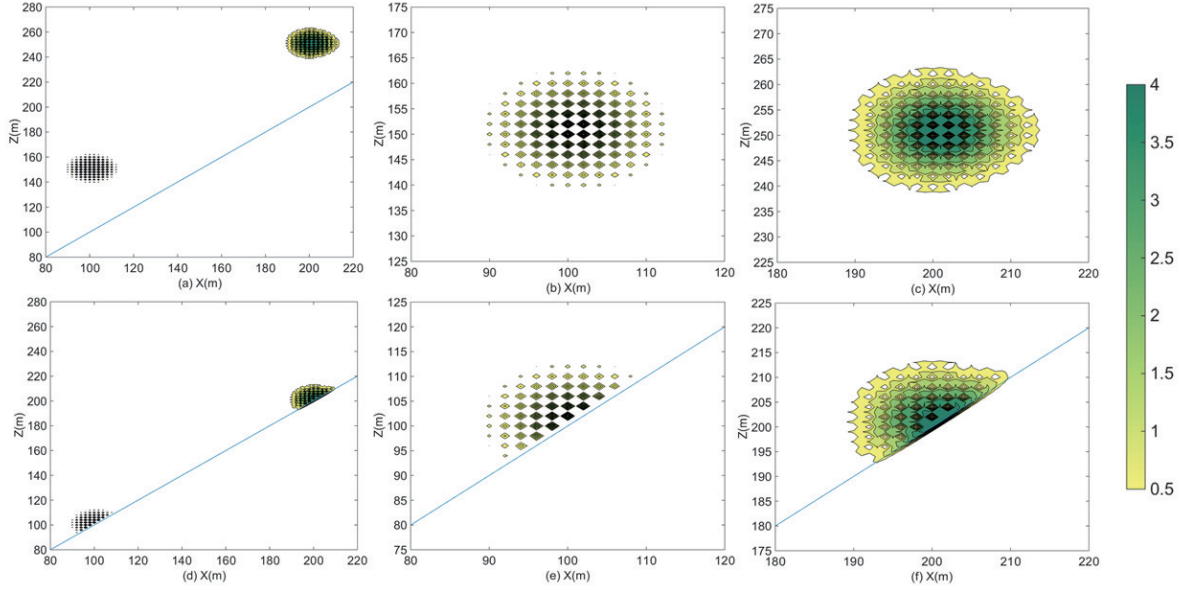


Fig. 10. 2D results of o2o3 with a cut-cell grid under a straight line representing the terrain. The tracer in the first row is above the terrain, while the tracer in the second row is advected along the terrain. The first column presents the initial values of the tracers and the advection results after 100 time steps. The second column shows magnified views of the field at the locations of the initial values. The third column shows magnified views of the forecast fields. (b) and (e) show a background comprising zero field values with clusters of higher values. These points are marked in white in Fig. 2 (b); as these points are unused for forecasting, they retain their initial values. (c) and (f) show a smooth structure representing the field. At some points corresponding to the points marked in white in Fig. 2 (b), there is a steep point valley assuming the value of zero. The contour interval is set to be 0.5.

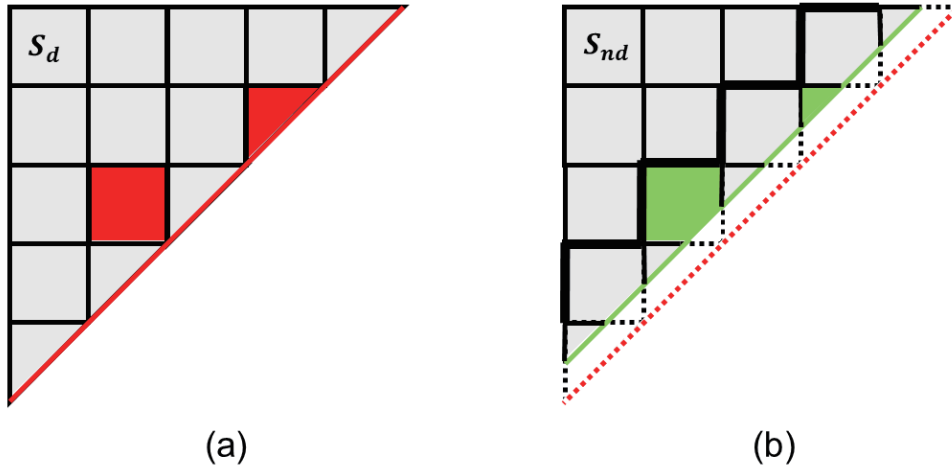


Fig. 11. Different options for the cut-cell grid. (a) Special case of a straight orographic line going through the cell corners, as was used in the example of Fig. 10. All cut cells in this case are triangular marked with red colors. (b) A general case where the orography does not cut each cell diagonally. The thick solid and green lines mark the boundary approximation cells. The cut cells are triangles or pentagons shown in green. The physical domains are the gray areas marked with S_d in (a) and S_{nd} in (b). The mass of the system is the integral of the density over the area above the orography. The polynomial field representations for the fluxes and the density can be uniquely extended to the whole area of the boundary approximation cells.

List of Tables

917	1	The properties of five numerical schemes (o2o3, o3o3, o4, SE2 and SE3).	62
918	2	The values of w_i in Eq. (12) on an irregular grid with resolution jumps.	63
919	3	The CFL conditions with RK4 time-stepping in the SE2, o2o3, SE3, centered FD and classic o4 schemes. The CFL condition with the spatial centered FD scheme is 2.8.	64
920			
921			
922			
923			

Table 1. The properties of five numerical schemes (o2o3, o3o3, o4, SE2 and SE3).

Property		o2o3	o3o3	o4	SE2	SE3
Order of polynomials	To field	2^{nd}	3^{rd}	/	2^{nd}	3^{rd}
Order of polynomials	To flux	3^{rd}	3^{rd}	/	2^{nd}	3^{rd}
Accuracy		$\geq 3^{rd}$	$\geq 3^{rd}$	4^{th}	2^{nd}	$\geq 3^{rd}$
Regularity of collocation grids within an element		Regular	Regular	Regular	Regular	Irregular
Mass conservation	Regular grid	Yes	Yes	Yes	Yes	Yes
Mass conservation	Irregular grid	Yes	Yes	No	Yes	Yes

Table 2. The values of w_i in Eq. (12) on an irregular grid with resolution jumps.

Resolution	w_i^{-1}	$w_i^{-\frac{1}{2}}$	w_i	$w_i^{+\frac{1}{2}}$	w_i^{+1}	Locations of point x_i
Fine Resolution ($dx = 1.0$)	0.083	-0.667	0.0	0.667	-0.083	$i = 1, 2, \dots, 177, 178$
Resolution Jumps	0.1	-0.75	0.167	0.5	-0.017	$i = 179$
Resolution Jumps	0.167	-1.067	0.75	0.167	-0.017	$i = 180$
Resolution Jumps	0.152	-0.5	0.083	0.3	-0.036	$i = 181$
Coarse Resolution ($dx = 2.0$)	0.042	-0.333	0.0	0.333	-0.042	$i = 182, 183, \dots, 207, 208$
Resolution Jumps	0.036	-0.3	0.083	0.5	-0.152	$i = 209$
Resolution Jumps	0.017	-0.167	-0.75	1.067	-0.167	$i = 210$
Resolution Jumps	0.017	-0.5	-0.167	0.75	-0.1	$i = 211$
Fine Resolution ($dx = 1.0$)	0.083	-0.667	0.0	0.667	-0.083	$i = 212, 213, \dots, 600$

Table 3. The CFL conditions with RK4 time-stepping in the SE2, o2o3, SE3, centered FD and classic o4 schemes. The CFL condition with the spatial centered FD scheme is 2.8.

Schemes	SE2	o2o3	SE3	centered FD	classic o4
CFL condition	2.2	1.8	1.5	2.8	1.9